Polarimetric Analysis of Biseasonal Monostatic and Bistatic Radar Observations of a Glacier Accumulation Zone at Ku-Band

Marcel Stefko, *Member, IEEE*, Philipp Bernhard, Othmar Frey, *Senior Member, IEEE*, and Irena Hajnsek, *Fellow, IEEE*

***Abstract*—We present ground-based Ku-band radar observations of the snow cover on top of the Great Aletsch Glacier carried out over two observation periods, in August 2021 and in March 2022. The observations were carried out with the combined mono/bistatic version of KAPRI, a full-polarimetric radar system, and revealed substantial differences between the scattering behavior of the snow cover between the two seasons. We analyze the spatial and temporal behavior of parameters, including temporal decorrelation, the scattering entropy, the mean polarimetric alpha angle, and the co-polarized phase difference (CPD) and the cross-polarized phase difference (XPD). The results indicate that snow cover decorrelates at Ku-band on the timescales of 4–12 h in winter and summer, which has implications for repeat-pass methods with long temporal baselines. The analysis of the CPD in winter indicates that the parameter is prone to phase wrapping. In summer, its value exhibits a smooth spatial trend and a strong sensitivity to changes in incidence angle and liquid water content. The bistatic XPD also acquires a nonzero value, indicating the presence of nonreciprocal scattering, which has implications for possible calibration procedures of bistatic systems. The presented results aim to serve as a reference for snow scattering behavior at Ku-band, which can aid planning of future data acquisition campaigns and satellite missions.**

***Index Terms*—Bistatic radar, interferometry, polarimetry, snow remote sensing.**

I. Introduction

A. Snow and Ice Investigations at Ku-Band

THE Ku-band frequency range of the electromagnetic spectrum (between 12 and 18 GHz) is attractive for radar investigations of snow and ice [1], [2], [3], [4]. This is due to the relatively short but nonzero penetration depth into dry snow, which allows a large fraction of the incident radio waves to interact with the snow volume, thus providing opportunities for probing of the physical properties of the snow layer, especially when the layer thickness is insufficient for use of lower frequency bands, such as the X-band [5], [6]. The snow parameters of interest include, among others, the snow water equivalent [2], [7], [8], grain size and autocorrelation length [9], [10], snow anisotropy [11], [12], or firn depth [13]. Several spaceborne synthetic aperture radar (SAR) missions using Ku-band for snow and ice research were proposed in the past decade (CoReH2O [14], SCLP [15, Part II]) and also are under current investigation (TSMM, [16]).

Manuscript received 4 February 2023; revised 5 June 2023, 12 October 2023, and 20 December 2023; accepted 20 February 2024. Date of publication 19 March 2024; date of current version 14 May 2024. *(Corresponding author: Marcel Stefko.)*

Marcel Stefko and Philipp Bernhard are with the Chair of Earth Observation and Remote Sensing, Institute of Environmental Engineering, ETH Zurich, 8093 Zurich, Switzerland (e-mail: stefko@ifu.baug.ethz.ch).

Othmar Frey is with the Chair of Earth Observation and Remote Sensing, Institute of Environmental Engineering, ETH Zurich, 8093 Zurich, Switzerland, and also with the GAMMA Remote Sensing AG, 3073 Gümligen, Switzerland.

Irena Hajnsek is with the Chair of Earth Observation and Remote Sensing, Institute of Environmental Engineering, ETH Zurich, 8093 Zurich, Switzerland, and also with the Microwaves and Radar Institute, German Aerospace Center, 82234 Weßling, Germany.

This article has supplementary downloadable material available at https://doi.org/10.1109/JSTARS.2024.3374051, provided by the authors.

Digital Object Identifier 10.1109/JSTARS.2024.3374051

B. Bistatic Radar Investigations of Snow

Bistatic radar (i.e., a radar measurement configuration where the transmitter (Tx) and the receiver (Rx) are spatially separated) is a technology that can potentially provide a complementary method of access to snow parameters to the widely used methods based on monostatic radar data (where the spatial separation of the transmitter and the receiver is negligible). It provides an opportunity to expand the observation parameter space, through variation of the bistatic angle β, which is defined as the spatial angle between the transmitter and the receiver from the point of view of the scatterer. Observations under varying values of β provide access, e.g., to a larger number of polarimetric parameters [17], [18]. This bistatic parameter space remains relatively unexplored, mainly due to bistatic radar's higher operational complexity as opposed to monostatic radar. The only bistatic spaceborne mission currently operating is TanDEM-X [19], whose bistatic capabilities were used to characterize snow both through investigations of the bistatic signal phase [20], [21], as well as bistatic intensity variations [22]. However, the nominal operational mode of TanDEM-X involves the use of very small bistatic angles (less than 1°). There are currently no bistatic spaceborne missions with larger bistatic angles. Ongoing interest in further development of bistatic radar missions is reflected in current proposals of spaceborne radar missions, such as Harmony [23], as well as past proposals [24], [25], [26], [27].

Modeling research of snow and ice has so far focused primarily on integrating passive and monostatic active radar observations [9], [10], [11], [12], [13], [28], [29], [30], [31]. However, it should be noted that many radar devices (even those conventionally considered monostatic, such as SnowScat [32])

have a nonzero spatial separation between the transmitting and receiving antenna. In certain cases (especially at short ranges), this separation can result in a bistatic angle value, which can nonnegligibly affect the observed backscatter, especially in volumetric scattering media such as snow [22, Sec. 4.3]. Polarimetric investigation of snow properties is also a subject of ongoing research [11], [13], [28], [31], [33], [34], [35], [36], [37], [38], [39], [40], [41].

C. Scattering Characteristics of Snow

Scattering characteristics of snow are strongly dependent on the properties of the incident radiation (frequency and polarization), physical parameters of the snow medium (grain size, water content, and layer parameters), as well as observation geometry (incidence, scattering angle). Extensive review literature is available on the topic, e.g., [4], [42], [43], [44], and [45]. In the following paragraphs, we shortly summarize the most relevant properties of snow with regard to our radar measurements.

Liquid water content has a strong effect on dielectric properties of snow, and thus strongly affects backscatter intensity, which becomes much weaker as water content increases. Furthermore, the penetration depth becomes much shorter with increasing water content due to absorption. This causes the majority of backscatter from wet snow to come from the uppermost layer of the medium with penetration depth on the order of only a few centimeters at Ku-band [46, Sec. 4.6], [47], and thus limits the possibilities of probing the deeper layers. Conversely, dry snow allows strong penetration of several meters at Ku-band [46, Fig. 4.15], and is a strongly scattering and weakly absorbing medium.

Seasonal snow often exhibits an anisotropic orientation of ice crystals and anisotropy of the large-scale structure, which can impose a polarization-dependent phase delay on the scattering waves [11]. The co-polar phase difference (CPD) [11], [13], [48] defined here as

$$\phi_{\mathrm{HH-VV}} = \phi_{\mathrm{HH}} - \phi_{\mathrm{VV}} = \arg(S_{\mathrm{HH}} S_{\mathrm{VV}}^{*}) \tag{1}$$

quantifies the difference between the phase of the horizontally polarized transmitted and received waves ϕ_{HH} and the vertically polarized equivalents ϕ_{VV}. The CPD is often used to characterize this polarization-dependent delay, and is strongly affected by changes in snow metamorphism and depth [11], [13]. Observations at L-band to Ku-band have been used to infer structural properties of the snow cover from CPD measurements [11], [13]. The short wavelength of the Ku-band makes the CPD very sensitive to small variations of these properties, however, it also makes it potentially prone to phase-wrapping already at layer depths of several tens of centimeters, especially at high incidence angles.

The cross-polarized phase difference (XPD) [49]

$$\phi_{\mathrm{HV-VH}} = \phi_{\mathrm{HV}} - \phi_{\mathrm{VH}} = \arg(S_{\mathrm{HV}} S_{\mathrm{VH}}^{*}) \tag{2}$$

quantifies the phase difference between the two crosspolarized channels, HV and VH. In the monostatic case, the reciprocity principle dictates that $S_{\mathrm{HV}} = S_{\mathrm{VH}}$, and thus, the XPD is zero by definition [50]. This fact is often used for calibration of cross-polarized channels [49]. However, in the bistatic case, the XPD does not necessarily need to be zero. Due to a low availability of bistatic full-polarimetric systems and datasets [51], the XPD has not been as thoroughly explored and modeled as its co-polarized counterpart. *Note:* Some publications may use the name "cross-polarized phase difference" for a different parameter, such as $\phi_{\mathrm{HV}} - \phi_{\mathrm{HH}}$ or similar (e.g. [52] and [53]). In this publication we use exclusively the definition in (2).

The two main scattering processes occurring in snow are surface scattering (from the air–snow boundary, snow–ground boundary, or internal layers, such as melt–freeze crusts), and volume scattering occurring throughout the snow volume [44]. Dihedral scattering can also occur from one or several of these boundaries. These processes have different polarimetric signatures—the 4-D Pauli scattering vector [17, Sec. 3.2, 6.5]

$$\mathbf{k}_{\mathrm{P}} = \frac{1}{\sqrt{2}} \begin{bmatrix} S_{\mathrm{HH}} + S_{\mathrm{VV}} \\ S_{\mathrm{HH}} - S_{\mathrm{VV}} \\ S_{\mathrm{HV}} + S_{\mathrm{VH}} \\ j(S_{\mathrm{HV}} - S_{\mathrm{VH}}) \end{bmatrix} \tag{3}$$

where S is the Sinclair scattering matrix and j is the imaginary unit, is often used to distinguish between these processes. Surface scattering exhibits a large magnitude of the first component $S_{\mathrm{HH}} + S_{\mathrm{VV}}$, whereas volume scattering exhibits a comparatively strong third component $S_{\mathrm{HV}} + S_{\mathrm{VH}}$. Dihedral scattering can manifest itself in the second $(S_{\mathrm{HH}} - S_{\mathrm{VV}})$ or third component, depending on the orientation of the scattering surfaces. The fourth component $j(S_{\mathrm{HV}} - S_{\mathrm{VH}})$ is always equal to zero in the monostatic case; however, in a bistatic measurement configuration it can have a nonzero value [17]. A graphical visualization of the Pauli scattering vector component magnitudes is often used for a qualitative analysis of scattering processes occurring within the snow medium (e.g., [54]). A quantitative analysis is often performed through second-order polarimetric parameters, such as the Cloude–Pottier scattering entropy H and polarimetric alpha angle α [17, Ch. 7], [55, Sec. 2.3], [56, Ch. 4], or the roll-invariant incoherent target decomposition [57], [58]. Use of these parameters is of interest, e.g., for terrain classification in snow-covered or frozen areas [39], [40], [41], [59], [60].

Snow is a medium that undergoes significant microstructural changes over time, with varying rates of change depending on snow type, snow cover age, and ambient conditions. [61] These changes significantly affect the scattering behavior, and can have a strong effect especially on the interferometric coherence γ and its temporal behavior, which are important for all radar interferometry-based observation methods. The complex interferometric coherence $\tilde{\gamma}$ is computed from two single-look complex (SLC) radar images s_1 and s_2 as follows:

$$\tilde{\gamma} = \frac{\sum_{\mathrm{W}} s_1 s_2^{*}}{\sqrt{\sum_{\mathrm{W}} s_1^2} \sqrt{\sum_{\mathrm{W}} s_2^2}} \tag{4}$$

where W is a boxcar moving window. Its final absolute value γ is constrained between 0 (no coherence) and 1 (full coherence). It is affected by several contributing factors, and can be expressed

as [19]

$$\gamma = \gamma_{\text{SNR}}\gamma_{\text{Quant}}\gamma_{\text{Amb}}\gamma_{\text{Rg}}\gamma_{\text{Az}}\gamma_{\text{Vol}}\gamma_{\text{Temp}}. \quad (5)$$

These terms, respectively, describe the reductions in coherence due to SNR, quantization, ambiguities, baseline decorrelation, relative shift of the Doppler spectra, volume decorrelation, and temporal decorrelation. The relevance of each individual term varies based on sensor type, observation geometry, and the observed medium. The final term γ_{Temp} is the temporal decorrelation between the two acquisitions, which in snow can occur due to, e.g., change of liquid water content (i.e., snowmelt or refreezing), or redistribution of the snow particles due to wind or displacement [62]. At Ku-band, scatterer displacement on the scale of 2–3 mm can already cause significant decorrelation [63, Eq. (23)]. Furthermore, temporal decorrelation can also be caused by glacier motion—even if the snow cover on top of the glacier remains stable, the motion of the glacier will over time cause the scatterers to move out of their original range cell, which will also cause the scene to decorrelate. This effect is strongly dependent on the observation parameters, namely, the range and azimuth sampling resolutions, and the orientation and rate of glacier flow with respect to the sensor. In general, the value of γ_{Temp} nonlinearly reduces with increasing time between acquisitions. Its temporal behavior can provide an upper bound on the realistic length of acquisition windows for repeat-pass methods, such as differential interferometry or SAR tomography, since after a certain time period, the two acquisitions will no longer be sufficiently coherent. Knowledge of the decorrelation time is thus vital, amongst other use cases, for planning and evaluation of viability of airborne and spaceborne data acquisition campaigns. This is especially true at Ku-band, since temporal decorrelation is generally faster at shorter wavelengths [62].

D. Terrestrial Radar Instruments for Snow Investigations

While this section focuses on ground-based instruments, airborne radar sensors (e.g., [31], [64], [65], [66], [67], [68], and [69]) are a powerful tool for snow monitoring. As opposed to terrestrial sensors, they usually provide superior spatial coverage, and can be easier to deploy in hard-to-access environments. However, they are usually more costly to operate, and offer only limited capabilities for long-term measurements with fine temporal resolution (i.e., maintaining regular sampling intervals over observation windows on the scales of days to months is difficult).

Comprehensive datasets using different radar imaging modalities in the cryospheric environment with very quick revisit times and virtually unlimited time-series durations can be acquired with terrestrial radar sensors. The following is a (nonexhaustive) list of terrestrial radar sensors employed for cryospheric investigations in the past decade:

1) The dual-frequency X-/Ku-band UW-Scat instrument analyzed seasonal backscatter trends of snow cover in relation to snow properties [5], [70].
2) As part of Phase A studies for the CoReH2O candidate mission, the NoSREx field experiment [3] carried out active and passive microwave measurements of snow. The active measurements spanning from 9.15 to 17.9 GHz were performed with the SnowScat instrument [32].
3) As part of the NASA SnowEx project, the SRT3 full-polarimetric radar performed X- and Ku-band observations of snow cover [71] and the observations were used for parameter retrieval [72], [73].
4) The SnowScat [47], [74], [75] and WBSCAT [76] scatterometers are used for measuring microwave signatures of snow in support of the ESA SnowLab project [77]. SnowScat covers the frequency range from 9.2 to 17.8 GHz, WBSCAT from 1 to 40 GHz. Both are used, among other purposes, to investigate the relationship between snow parameters and the corresponding detected radar characteristics, and for tomographic profiling.
5) The terrestrial Ku-band radar system KAPRI is capable of bistatic full-polarimetric interferometric imaging of areas kilometers in size [78]. It is based on the terrestrial interferometer Gamma GPRI [79], [80], [81], [82]. Its bistatic capabilities were previously applied to investigate the occurrence of the coherent backscatter opposition effect in seasonal snow [22]. It was also previously used (in the monostatic configuration) to monitor the Alpine glacier Bisgletscher in the context of a geostatistical analysis of the spatial and temporal behaviors of the atmospheric phase screen (APS) in Ku-band [83], [84], as well as polarimetric analysis of natural terrain [85].

E. Contributions of This Article

In August 2021 and March 2022, we carried out time series observations of the Jungfraufirn area of the Great Aletsch Glacier in Switzerland with KAPRI, acquiring a fully polarimetric interferometric time series of both monostatic and simultaneous bistatic observations of the glacier's accumulation zone. In this article, we

1) describe the acquisition setup and the acquired data;
2) describe the data processing pipeline, including an updated range correction method to correctly geocode data in the complicated bistatic radar geometry, and to compensate for the topographic phase;
3) analyze the temporal decorrelation behavior of snow cover at Ku-band, including development of a simple model to estimate the effect of glacier drift;
4) analyze the observed polarimetric characteristics of the snow cover (both monostatic and bistatic), and their spatial and temporal variation;
5) discuss the observed Ku-band scattering behavior and its implications for multistatic monitoring and modeling of snow and ice at Ku-band.

The rest of this article is organized as follows. Section II describes the observation site and ambient conditions during the measurements, the methodology of the multistatic radar acquisition setup, processing and calibration, in-situ data collection, and data analysis. Section III analyzes the resulting data, namely, the spatial and temporal behavior of coherence (including an assessment of influence of glacier drift), scattering entropy, mean alpha angle, and CPDs and XPDs, both in monostatic and bistatic

Fig. 1. Photos of both devices deployed at the High Altitude Research Station Jungfraujoch complex. The primary device (top) was deployed on top of the Research Station terrace, and the secondary device (bottom) was deployed on the terrace of the East Ridge (*Ostgrat*) building. Both devices observe the Jungfraufirn area, visible in the background of both images. The synchronization antennas pointed along the bistatic baseline are visible in bottom right and top left parts of the two images, respectively. The pointing directions of the antennas within the images are approximately south and south-east for the primary and secondary devices, respectively.

geometries. A discussion of the behavior of these parameters and the possible underlying causes is given in Section IV. Finally, Section V concludes this article.

II. Methods

A. Radar Observations

An in-depth description of the bistatic KAPRI system used for the observations can be found in [78]. The two devices were deployed on two terraces of the High Altitude Research Station Jungfraujoch, both with direct line-of-sight to the ROIs in the Jungfraufirn area of the Great Aletsch Glacier, and with direct line of sight between each other for synchronization purposes. Photographs of the two devices are shown in Fig. 1. A map of the observed area with marked positions of devices and observed scene is shown in Fig. 2. Due to the altitude difference between the positions of the two devices forming the bistatic configuration, a special bistatic range shift procedure needed to be developed in order to align the monostatic and bistatic datasets. This procedure is described in detail in Section S-I of the Supplementary Material. The details of polarimetric calibration of the two devices are described in Section S-II of the Supplementary Material.

TABLE I
Radar Acquisition Parameters and Temperature Conditions During Acquisition Campaigns

Period	summer	winter
Date (D+0)	19 August 2021	2 March 2022
Time span (UTC)	04:15 – 08:15 17:50 – 05:15 (D+1)	09:00 – 15:40 (D+1)
Angular sweep	1 deg/s	2 deg/s
Repetition time	∼3 min	∼2 min
FMCW chirp length	4 ms	
Bandwidth	200 MHz	
Polarization	Full-pol (HH, HV, VH, VV)	
Modality	Monostatic + bistatic	
Temperature (max)	4 °C	−10 °C
Temperature (min)	−2 °C	−15 °C

The (D+1) mark indicates that the time stamp corresponds to the day following the start date of the acquisition period.

The radars performed repeated acquisitions over the acquired area, with repetition times on the order of $2-4$ min. The winter acquisition spanned ~ 30 h, whereas the summer acquisition spanned ~ 25 h. In summer, for logistical reasons there is a ~ 9.5-h interval during the day in which no acquisitions were made. The key parameters of the radar observation periods are summarized in Table I. The instruments were operated with similar configuration during both periods; however, a faster azimuthal sweep velocity was chosen in winter, in order to ensure smooth operation of the moving parts at low temperatures—this results in shorter integration time in winter and an associated reduction of SNR (of expected magnitude of 3 dB) as compared with the summer configuration.

B. Area Description and In-Situ Data

The observed area is situated in the area of the Jungfraufirn, one of the three main tributaries of the Great Aletsch Glacier, which is the largest alpine glacier in the European Alps. It exhibits location-dependent typical flow rates of 20–80 cm/day [21], with annual surface velocity averages up to 200 m/year [86]. The observed area spans altitudes between 2800 and 3600 m asl, with the equilibrium line of the glacier (averaged between years 1865–2006) at approx. 3000 m asl [87].

No fresh snowfall events occurred during the summer nor the winter campaign. As shown in Table I, snow melt was occurring during summer due to above-zero temperatures. In winter, temperatures remained well below zero and no snow melt was observed. Weather station data from a nearby automated meteostation during the observation periods can be found in Fig. S2 of the Supplementary Material.

Several snow pits were dug over the course of the winter campaign, and vertical profiles of snow density, temperature, and grain size were acquired. The location of snow pits is shown in Fig. 2. In summer no snow pits were dug due to logistical reasons. In summer the snow cover showed to be hard, recrystallized and firn-like, caused by repeated melt-freeze events over the course of the preceding season. In winter, snow pits revealed a fresh seasonal snow layer of more than 2 m depth at each site. Snow pit data showing the vertical profiles of snow grain size, density, and temperature acquired over the course of the

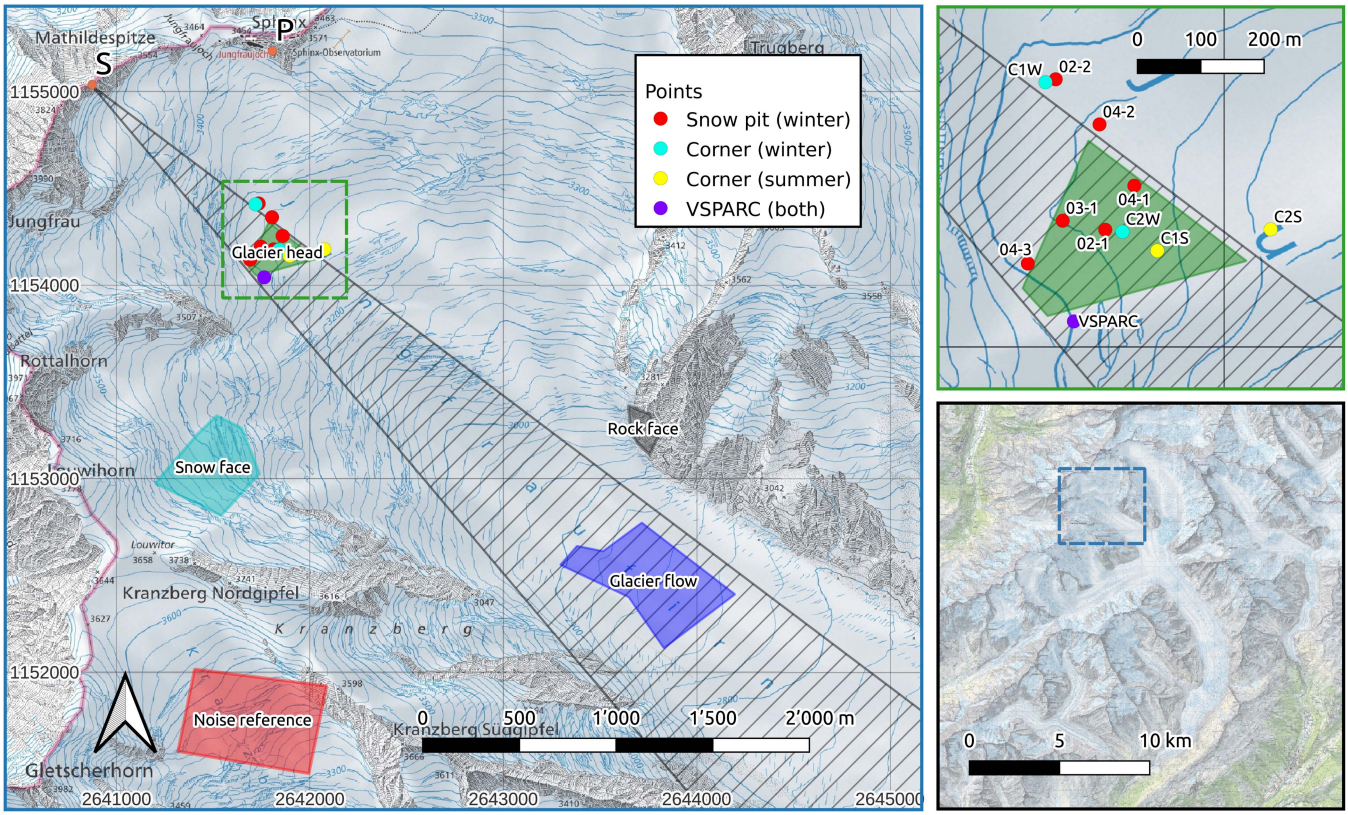

Fig. 2. Map of the observed area of the Jungfraufirn region of the Great Aletsch Glacier. In the left map, the positions of the primary and secondary radar are marked in the top left of the figure as P and S, respectively. The ROIs are marked as colored polygons. The locations of the six snow pits are marked as red points. C1S, C2S and C1W, C2W mark the positions of the two reference corner reflectors in summer and winter, respectively. VSPARC denotes the position of the active radar calibrator. The patterned triangle denotes the coverage of the secondary receiver's antennas (i.e., bistatic coverage). The coordinate grid of the left map corresponds to the CH1903+/LV95 coordinate system (EPSG:2056). The two smaller maps on the right side of the figure, respectively, show a zoomed-in detail of the "Glacier head" ROI area (top), and an overview of the position of the campaign site within the Great Aletsch Glacier region (bottom). Precise extents of the individual subregion maps can be identified as hashed rectangles with color corresponding to the subregion map's outline color.

TABLE II
DESCRIPTION OF ROIS

ROI label	Surface type	Approx. range	Bist. coverage	β
Glacier head	Snow	800 m	Yes	$\sim 40°$
Glacier flow	Snow	3000 m	Yes	$\sim 10°$
Rock face	Rock	2500 m	No	N/A
Snow face	Snow	2000 m	No	N/A

winter campaign can be found in Fig. S3 of the Supplementary Material. An exemplary photo of the snow pit is shown in Fig. S4 of the Supplementary Material.

C. Regions of Interest (ROI)

For the time series analysis, several ROIs were defined, encompassing different parts of the observed scene. The ROIs are shown in Fig. 2 and described in Table II. Due to the limited coverage of the bistatic receiver's antennas, bistatic data is only available from two of the ROIs. During certain periods of both summer and winter campaigns, a corner reflector was placed within the "Glacier head" ROI for purposes of polarimetric calibration. To avoid biasing the measurements, the placement locations of the corner reflector were masked out from the dataset before polarimetric/coherence analysis.

D. Temporal Coherence Analysis

In order to explore the behavior of temporal decorrelation γ_{Temp}, the contribution of all other effects in (5) needs to be quantified. Several of these terms (described in-depth in [19]) can be neglected due to the setup of the measurement—zero volume decorrelation can be assumed since there is zero spatial baseline between the individual repeat-pass measurements ($\gamma_{\text{Vol}} \approx 1$) [88]. Due to the high bit depth of the receiver's ADC (14 bits/sample), quantization error [89] can also be neglected ($\gamma_{\text{Quant}} \approx 1$).

Range and azimuth ambiguities can have a contribution toward biasing of coherence through the term γ_{Amb}. Such ambiguities would also appear coherently in all interferograms, and could thus bias the coherence estimates. The magnitude of their effects on coherence can be approximated by [19, Eq. (26)]

$$\gamma_{\text{Amb}} = \frac{1}{(1+\text{RASR})(1+\text{AASR})} \tag{6}$$

where RASR and AASR are the range and azimuth ambiguity-to-signal ratios, respectively.

Range ambiguities in an FMCW radar could be caused if the pulse repetition interval is too short and echoes from multiple consecutive chirps pass through the band-pass filter simultaneously. To avoid this, the FMCW chirp length $\tau = 4\,\text{ms}$ was set sufficiently long so that no areas within direct line of sight to the radar system can cause such a phenomenon. Furthermore, topography-caused multipath effects could cause presence of range ambiguities in particular scenarios, such as when the ROI is on a face of a hill, and a flat plateau is present between the radar and the ROI [90]. In this experiment, most ROIs do not satisfy this condition and, thus, no multipath effects are expected. One possible exception could be the "Snow face" ROI, since a flat plateau is present between the primary device and the ROI (approximately around the location of the "Glacier head" ROI). While the "Snow face" ROI has a stronger radar brightness as opposed to the plateau due to a steeper local incidence angle, which should mitigate the effect, a certain degree of influence of multipath scattering on coherence estimates of the "Snow face" ROI can not be definitively excluded. This needs to be kept in mind for coherence analysis of the "Snow face" ROI. The coherence estimates in other ROIs are not affected, and for these ROIs the range ambiguities can be assumed as negligible (RASR ≈ 0).

The primary device's antennas have a one-way peak sidelobe ratio (PSLR) of $-15\,\text{dB}$. For the primary device, this ratio is applied both ways, resulting in negligible coherence loss

$$\text{AASR}_{\text{mono}} = -30\,\text{dB} \Rightarrow \gamma_{\text{Amb,mono}} = \frac{1}{1+10^{-3}} > 0.99. \quad (7)$$

In the bistatic case, the return path provides no sidelobe attenuation, thus, the estimated decorrelation is

$$\text{AASR}_{\text{bist}} = -15\,\text{dB} \Rightarrow \gamma_{\text{Amb,bist}} = \frac{1}{1+10^{-1.5}} \approx 0.97. \quad (8)$$

This value is also negligible compared with the remaining terms and can, thus, be neglected ($\gamma_{\text{Amb}} \approx 1$). Azimuth ambiguities stronger than those calculated above (7) and (8) could be present when imaging dark regions situated close to much brighter scatterers (such as corner reflectors), due to the sidelobes of the real-aperture antennas. The area around the corner reflectors placed in the "Glacier head" ROI was masked out from corresponding monostatic data before coherence analysis, in order to avoid biasing the ROI coherence estimates by their scattering response. The ROIs are, thus, not expected to be affected by especially bright azimuth ambiguities, as there were no comparatively brighter scatterers within their vicinity.

1) Glacier Drift: Due to the real-aperture nature of the measurement there is zero shift of the Doppler spectra, and due to zero spatial baseline the incidence angle on flat surfaces remains constant. The only factor affecting terms γ_{Rg} and γ_{Az} is, thus, possible miscoregistration of datasets. This misregistration can be caused by glacier drift over time, since it can cause scatterers to move out of their original range cell. We can introduce a term

$$\gamma_{\text{Drift}} = \gamma_{\text{Rg}}\gamma_{\text{Az}} \quad (9)$$

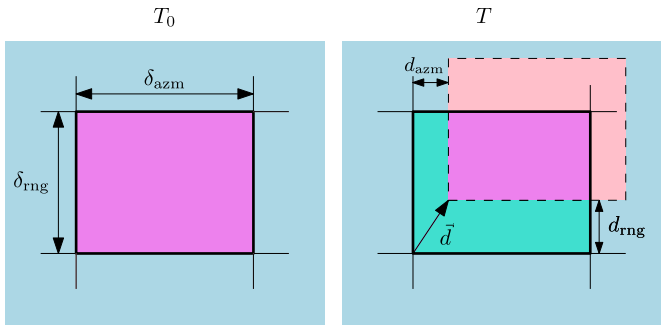

Fig. 3. Linear model visualizing the relationship between glacier drift $\vec{d} = (d_{\text{rng}}; d_{\text{azm}})$ and the coherence loss γ_{Drift}. At time T_0, all original scatterers (violet) are present in the range cell, thus, $\gamma_{\text{Drift}} = 1$. As the glacier drifts, part of the original scatterers depart the range cell (light pink), whereas new scatterers enter the range cell (cyan). The drift coherence factor γ_{Drift}, thus, reduces according to (9), (10), and (11).

which represents the drop of temporal coherence between times T_0 and T, which occurs when glacier displacement along range and azimuth d_{rng} and d_{azm} accumulates a nonnegligible value compared with the resolution cell dimensions δ_{rng} and δ_{azm}. The value of γ_{Drift} starts at 1 when $T = T_0$, and reduces to 0 once drift causes all the original scatterers to leave the range cell. Fig. 3 visualizes this phenomenon. The values of γ_{Rg} and γ_{Az} can be approximated as [19]

$$\gamma_{\text{Rg}} \approx \text{sinc}\left(\pi \frac{d_{\text{rng}}}{\delta_{\text{rng}}}\right) \quad (10)$$

and equivalently for the azimuth shift

$$\gamma_{\text{Az}} \approx \text{sinc}\left(\pi \frac{d_{\text{azm}}}{\delta_{\text{azm}}}\right). \quad (11)$$

Thus, if it is not possible to correct the drift effect by precise coregistration, its influence can be arbitrarily mitigated by decimation of the SLC (i.e., increasing the resolution cell dimensions through downsampling), which increases δ_{rng} and/or δ_{azm}.

Glacier drift rate can be estimated from KAPRI data using repeat-pass differential interferometry, provided that the temporal sampling rate is dense enough to avoid phase unwrapping errors caused by rapid drift of APS variations. The drift along the slant-range direction $d_{\text{slant-range}}$ is related to total horizontal drift d_{horiz}:

$$d_{\text{horiz}} = \frac{d_{\text{slant-range}}}{\cos\phi_{\text{drift}} \sin\theta_{\text{inc}}}. \quad (12)$$

In this equation ϕ_{drift} is the angle between the slant-range look vector and the glacier drift vector, and θ_{inc} is the incidence angle.

KAPRI's nondecimated range sampling resolution is 0.75 m. Using a range decimation factor of 6, the effective range cell size is increased to $\delta_{\text{rng}} = 4.5\,\text{m}$. The azimuthal width of the range cell is range-dependent (due to the real aperture). Using a beamwidth of 0.35 ° the width within the ROIs (which are placed at ranges above 800 m) is 5 m or more. An azimuthal decimation factor of 2 will thus result in the range cell width $\delta_{\text{azm}} \geq 10\,\text{m}$.

In this publication, we are investigating temporal coherence decays on scales of less than 24 h. Based on our own data (see Section III-A) as well as satellite measurements [21], we

estimate the worst-case drift values for both range and azimuth as $D_{\max} \approx 0.25\,\mathrm{m}$. We can thus consider the glacier drift effect nonnegligible over temporal baselines longer than several hours, if nondecimated data is used ($\delta_{\mathrm{rng}} = 0.75\,\mathrm{m}, \delta_{\mathrm{azm}} \geq 5\,\mathrm{m}$). Using a $6\times$ range decimation factor and a $2\times$ azimuth decimation factor, the upper ceiling of the effect of glacier drift on temporal coherence after 24 h can be estimated as a negligible value of

$$\gamma_{\mathrm{Drift,24\text{-}h}} = \mathrm{sinc}\left(\pi \frac{0.25\,\mathrm{m}}{4.5\,\mathrm{m}}\right) \mathrm{sinc}\left(\pi \frac{0.25\,\mathrm{m}}{10\,\mathrm{m}}\right) > 0.99. \quad (13)$$

For comparison, using nondecimated data would result in a 24-h drift coherence loss of $\gamma_{\mathrm{Drift,24\text{-}h}} = 0.82$—this would cause a 20% underestimate of coherence within ROIs located on the glacier, thus potentially overestimating temporal decorrelation rates, which are discussed in the next section.

2) Temporal Decorrelation: The two remaining terms have the biggest impact on the coherence of the measurement:

$$\gamma \approx \gamma_{\mathrm{SNR}} \gamma_{\mathrm{Temp}}. \quad (14)$$

The SNR term varies greatly depending on range distance, local incidence angle, and scattering properties. Its value can be estimated from the data by dividing the multilooked intensity by the noise floor. Then, the decorrelation due to noise can be estimated as [91]

$$\gamma_{\mathrm{SNR}}[T_1, T_2] = \frac{1}{\sqrt{(1 + \mathrm{SNR}_{T_1}^{-1})(1 + \mathrm{SNR}_{T_2}^{-1})}} \quad (15)$$

where SNR_T denotes the signal-to-noise ratio of the acquisition taken at time T. This ratio can change over time in case of changes in the observed scene (such as snowmelt/refreezing), or changes in the receiver (e.g., thermal drift). The temporal evolution of the temporal decorrelation starting at time T_0 can, thus, be estimated from the observed coherence $\gamma[T_0, T]$ as

$$\gamma_{\mathrm{Temp}}[T_0, T] \approx \frac{\gamma[T_0, T]}{\gamma_{\mathrm{SNR}}[T_0, T]}. \quad (16)$$

Assuming that γ_{SNR} and γ_{Temp} are uncorrelated, one can apply the variance formula for error propagation [92] to (14) and derive

$$\Delta\gamma_{\mathrm{Temp}} \approx \frac{\sqrt{\Delta\gamma^2 - \gamma_{\mathrm{Temp}}^2 \Delta\gamma_{\mathrm{SNR}}^2}}{\gamma_{\mathrm{SNR}}} \quad (17)$$

where $\Delta\gamma_{\ldots}$ signifies the error estimate of $\gamma_{\ldots}$. This indicates that when SNR is low (and, thus, γ_{SNR} is low, such as at high ranges or in the bistatic regime), the uncertainty of the γ_{Temp} estimate diverges.

E. Reciprocity Principle Considerations

Due to the reciprocity principle, in the monostatic case the cross-polarized channels HV and VH should be equal, i.e., $S_{\mathrm{HV}} = S_{\mathrm{VH}}$. This fact has been long-used to simplify polarimetric relations by reducing the dimensionality of the data [17], [55], [56], and can also be used for, e.g., calibration [93] or noise filtering [94]. However in the bistatic case the principle no longer generally applies, and in general S_{HV} and S_{VH} do not need to be equal. It is, therefore, of interest to investigate the (possibly nonzero) additional polarimetric parameters. These parameters include the cross-polar phase difference $\phi_{\mathrm{HV-VH}}$, the cross-polar intensity ratio $I_{\mathrm{HV}}/I_{\mathrm{VH}}$, or the fourth (i.e., smallest) eigenvalue λ_4 of the coherency matrix T [17], [94]

$$T = \langle \mathbf{k}_{\mathrm{P}} \cdot \mathbf{k}_{\mathrm{P}}^{\dagger} \rangle. \quad (18)$$

F. Sign of the Phase Differences

The sign convention of the polarimetric phase differences is important to define for their proper interpretation and comparison with other literature. In a typical radar processing workflow there are several possible ways the sign of the phase can be flipped (and thus differ between publications), from the choice of coordinate systems (FSA versus BSA) [17], [56], definition of the phasor rotation direction with increasing range, or ordering of the terms in definitions of phase differences (cf. e.g., [13], [31], [95], which use the HH–VV ordering, and [11], [48], [96], [97] where VV–HH ordering is used).

In this publication, the phase ϕ is defined to decrease with increasing range of the scattering target, i.e., when a target increases its distance from the sensor, the phase of its scattering response decreases:

$$\phi(r) = -\frac{4\pi}{\lambda} r. \quad (19)$$

The implication for polarization phase differences is that if the HH phase center is further away from the radar sensor along range direction as opposed to the VV phase center, and phase wrapping does not occur, the CPD will be negative. For example, if the HH phase center is further away by range distance $\lambda/8$, the resulting CPD according to (1) will be $\phi_{\mathrm{HH-VV}} = \phi_{\mathrm{HH}} - \phi_{\mathrm{VV}} = -\pi/2$. The same applies for XPD for HV and VH phase centers, respectively.

III. Data and Results

To provide a reference frame for interpretation of polarimetric data, in Fig. 4 we show the Pauli RGB representation of backscatter images for the morning of both seasons, for both monostatic and bistatic data. Fig. 5 shows the time series of estimated SNR (i.e., radar brightness β_0 divided by the noise floor) for each ROI defined in Table II. The data shows that the bistatic dataset, especially the "Glacier flow" ROI, exhibits very low SNR once snowmelt sets in in summer. The bistatic SNR in the winter season in this ROI is also low. Care, thus, has to be taken when interpreting bistatic observations in this region, since noise will have considerable influence.

A. Glacier Drift and Temporal Coherence

In order to validate the drift estimates described in Section II-D1, we estimated the glacier drift in the ROIs from monostatic KAPRI observations using differential interferometry. Fig. 6 shows the slant-range drift rate for both seasons estimated by unwrapping the differential interferometric phase. The slant range drift rate in the glacier ROIs is estimated at approx. 25 cm/day. For the "Glacier flow" ROI, this estimate is close to the total drift value, since the incidence angle is very shallow and the glacier flow direction is oriented along range. For the "Glacier head ROI," we can assume that the drift vector has an approximately 45° angle ϕ_{drift} with the range direction. We

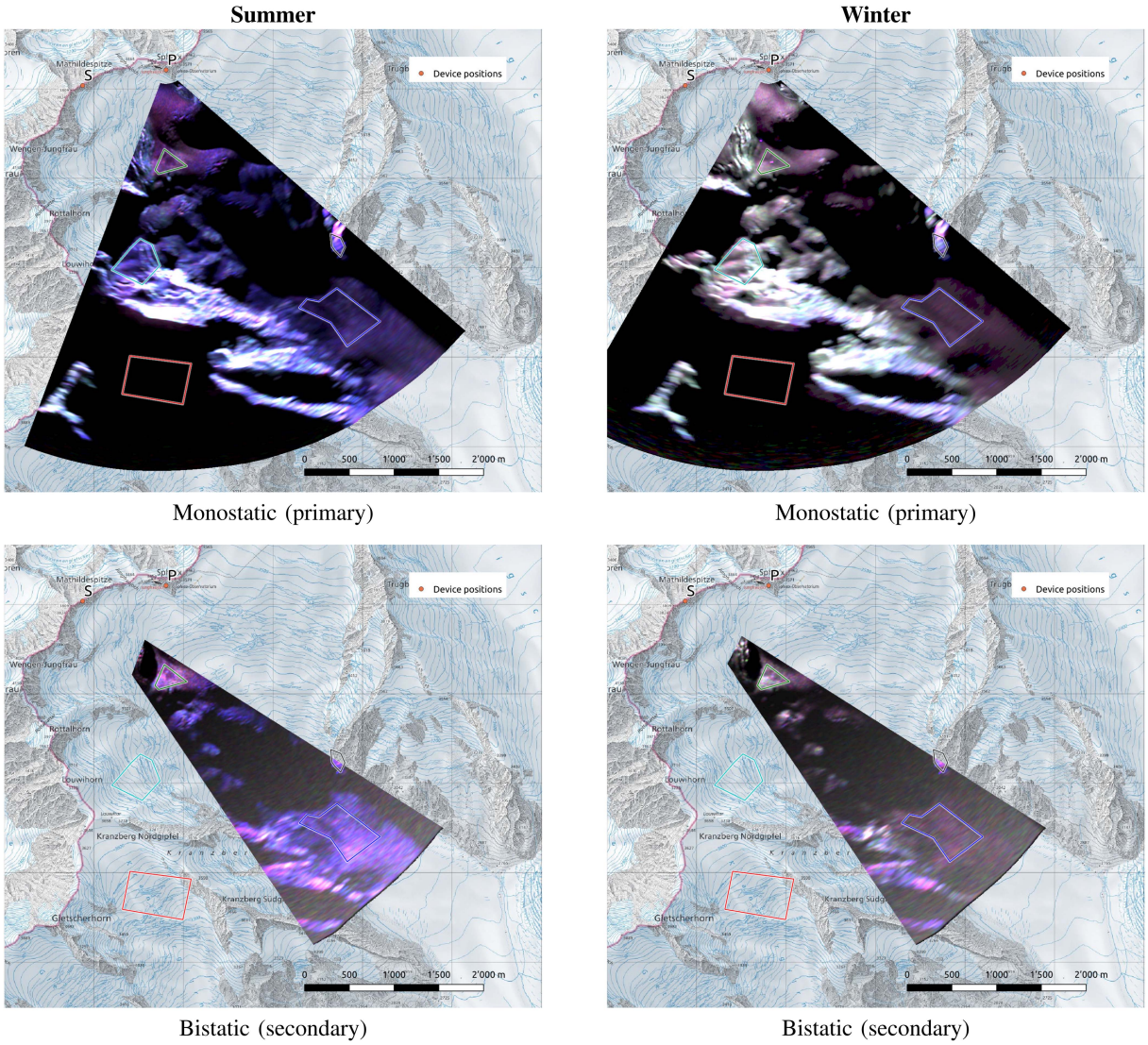

Fig. 4. Comparison of the Pauli representation (B:HH+VV, R:HH-VV, G:HV+VH) of polarimetric data for the summer (left) and winter (right) seasons, showing both monostatic (top) and bistatic (bottom) data. The gamma-scaling of each image was individually adjusted for better contrast and feature visibility. Bistatic images were cropped to show only the area covered by the main lobe of the secondary receiver antennas. The images show that backscatter behavior is dramatically different between the two seasons. The predominantly blue color of summer acquisitions indicates dominance of surface-type scattering, whereas the mixed color of winter acquisitions indicates a higher diversity of scattering processes. The reduced SNR of bistatic images due to use of lower-gain antennas is visible as noise in the far-range regions of the images.

TABLE III
DRIFT VALUES OVER A 24-H PERIOD ESTIMATED FROM KAPRI DIFFERENTIAL INTERFEROMETRIC MEASUREMENTS (SEE FIG. 6). THE DIFFERENCE BETWEEN SUMMER AND WINTER VALUES IS NEGLIGIBLE FOR PURPOSES OF ESTIMATION OF DRIFT EFFECTS ON COHERENCE.

ROI label	ϕ_{drift}	$d_{\text{slant range}}$	d_{horiz}	d_{rng}	d_{azm}
Glacier head	45°	23 cm	33 cm	23 cm	23 cm
Glacier flow	0°	21 cm	22 cm	22 cm	0 cm

can, thus, compute the total drift and the drift components along azimuth and range using (12). Table III shows the calculated displacement values along range and azimuth for the two glacier ROIs.

The drift estimates were then used to assess the influence of range cell drift on temporal coherence estimates and apply decimation in order to mitigate this effect (Section II-D1). Fig. 7 shows the resulting time series of estimation of temporal coherence $\gamma[T_0, T]$ for the two seasons, with the reference time of day T_0 chosen in the evening of each observation period, in order to avoid further snow melt and maximize time series span. Fig. S5 of the Supplementary Material shows the maps of this observed coherence $\gamma[T_0, T]$ over spans of approximately 2, 4, and 8 h, for the summer and winter seasons, respectively.

B. Second-Order Polarimetric Parameters

For a high-level characterization of scattering processes occurring within the observed areas at Ku-band, and their temporal

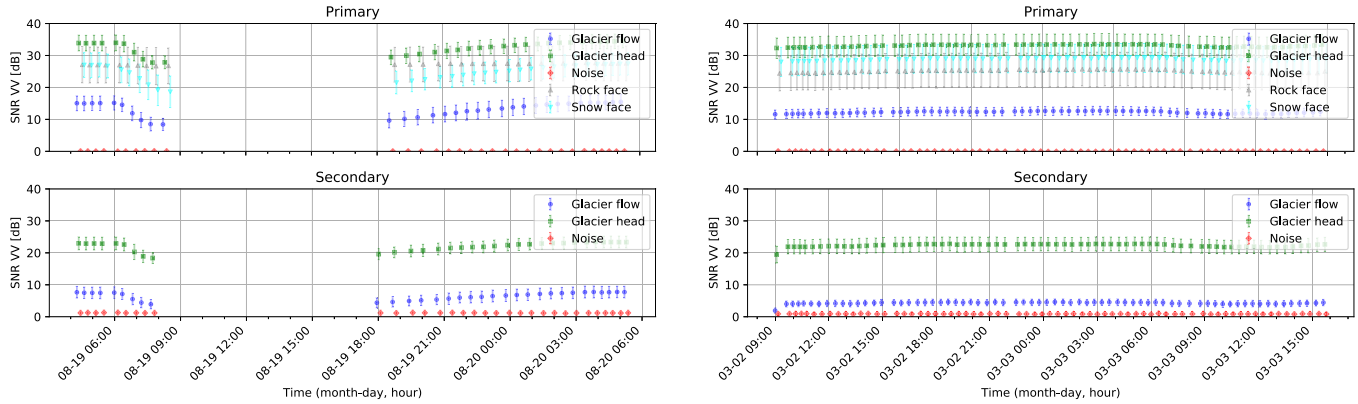

Fig. 5. Time series of SNR in the VV polarization for summer (left) and winter (right) seasons, for both monostatic (top) and bistatic (bottom) data, per ROI. The noise reference level was derived as the mean intensity of all areas with single-pass interferometric coherence $\gamma < 0.1$. The bistatic SNR is in general lower than monostatic SNR due to use of lower gain antennas. In summer, snowmelt during the day causes additional reduction of SNR, leading to critically low SNR values in the "Glacier flow" ROI of $< 5\,\mathrm{dB}$.

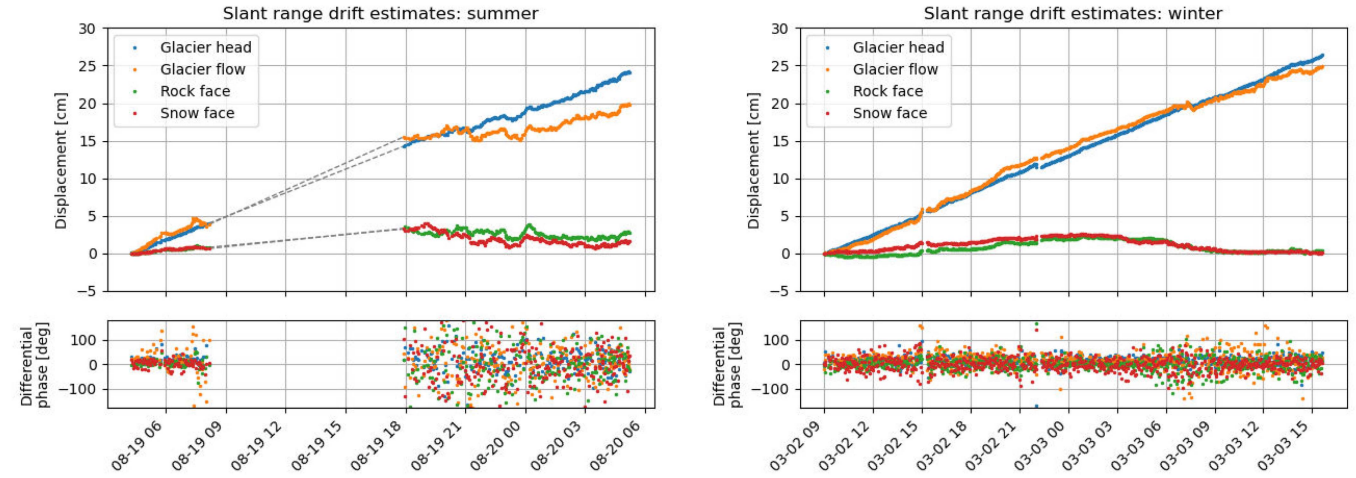

Fig. 6. Slant-range glacier drift of the glacier within individual ROIs estimated from the monostatic radar data by differential interferometry. The drift during the sampling gap in the summer dataset is linearly extrapolated (dashed lines) from the preceding observations. The winter dataset (sampled at 2 min) shows stable drift of approx. 21 cm/day. In the summer dataset, stronger phase variance is observed. This can be explained by more turbulent atmospheric conditions, lower SNR (see Fig. 5), and a longer sampling rate of approx. 3–4 min. This can cause possible phase wrapping, which likely leads to underestimation of the final drift estimate value, especially for the further-placed "Glacier flow" ROI. However, extrapolation of the initial, stable part of the drift curve results in a summer drift estimate of approx. 23 cm/day.

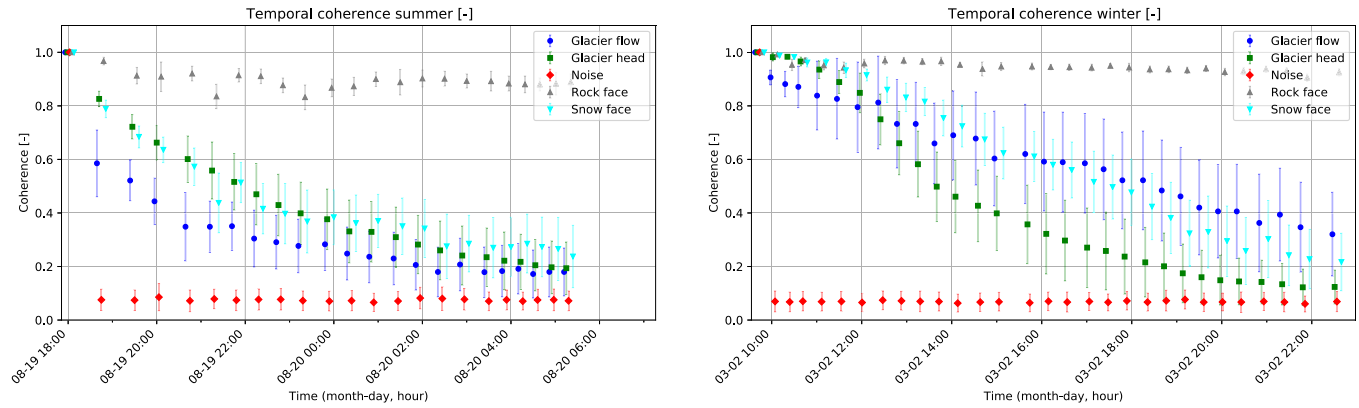

Fig. 7. Time series of coherence $\gamma[T_0, T]$ for the summer (left) and winter (right) seasons. Time T_0 in summer was chosen in the evening to avoid the increase of liquid water content during the day, and to maximize the uninterrupted time series length. Due to stability of the scene in winter, the choice of T_0 has negligible impact on data in winter. For both seasons, the time axis spans 13 h. The points and error bars represent the mean and the standard deviation of the coherence within each ROI.

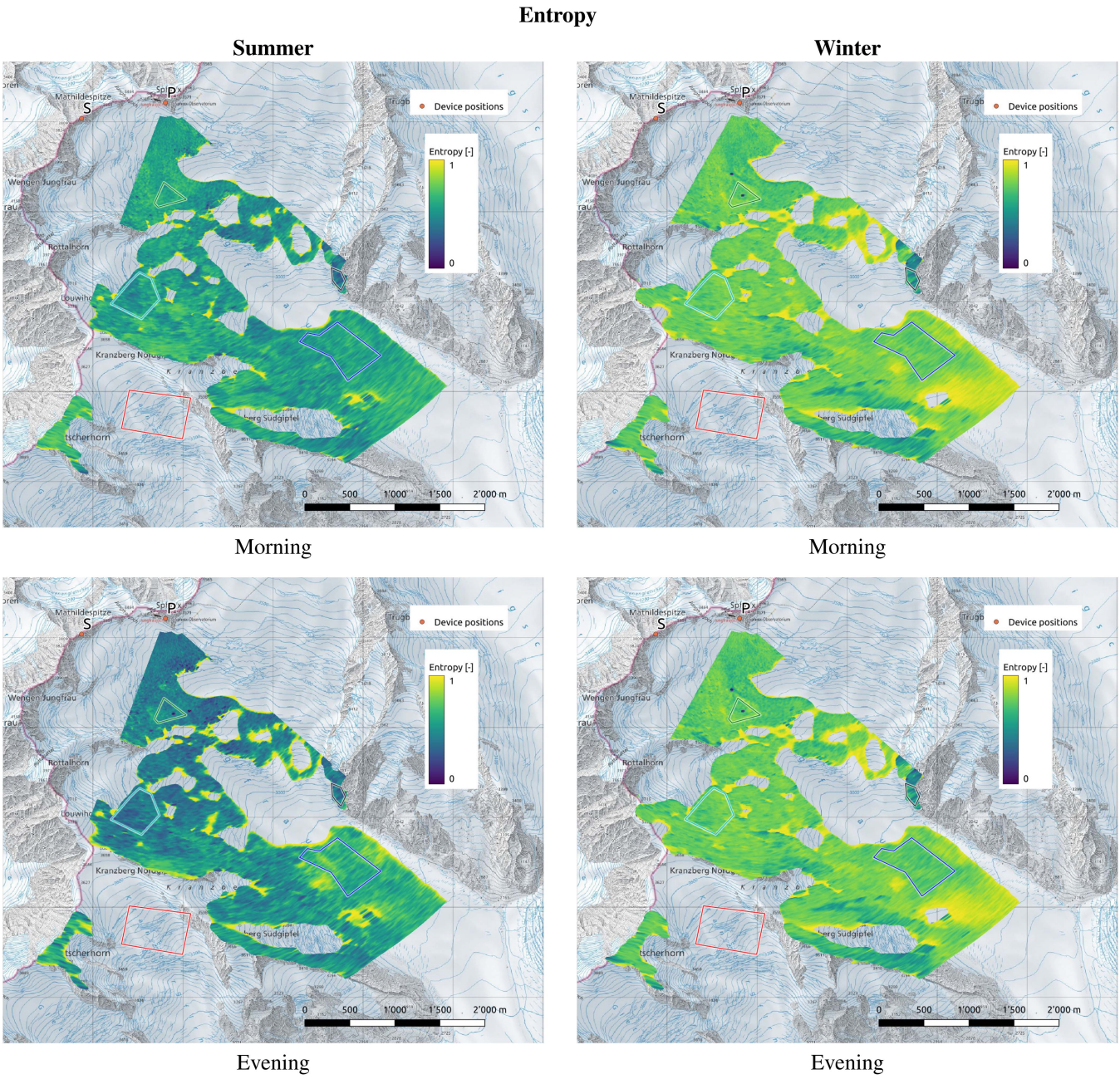

Fig. 8. Comparison of the observed monostatic entropy H for the summer (left) and winter (right) seasons, for morning (top) and evening (bottom) times of day. In winter, the entropy retains a high value throughout the day. In summer, entropy is comparably lower. It also further reduces during the day and reaches its minimal value after sunset. The exception are exposed rock areas, which retain a low entropy value throughout.

evolution, we investigate closer the second-order polarimetric parameters, specifically the scattering entropy H and the mean alpha angle $\bar{\alpha}$. The parameters were computed from the coherency matrix T [see (18)] which was computed using a 5×5 spatial averaging window.

The scattering entropy H can serve as a measure of the diversity of scattering processes [17, Ch. 7]. Fig. 8 shows the value of entropy in the monostatic dataset for morning and evening of each season. For brevity, maps of these parameters for the bistatic dataset are not shown, however, the bistatic behavior can be assessed through investigation of the time series—this is shown in Fig. 9 and shows monostatic and bistatic values of these parameters for each ROI as specified in Fig. 2. This data shows a large difference between the entropy behavior in summer and in winter. Furthermore, entropy exhibits intraday variation in summer, whereas in winter it remains stable throughout the whole observation period, for both monostatic and bistatic datasets.

For an assessment of the type of dominant scattering mechanism [56, Sec. 4.1.3], [17, Ch. 7], Figs. 10 and 11 correspondingly show the maps and time series for the mean alpha angle $\bar{\alpha}$. Behavior similar to scattering entropy H is observed, where $\bar{\alpha}$

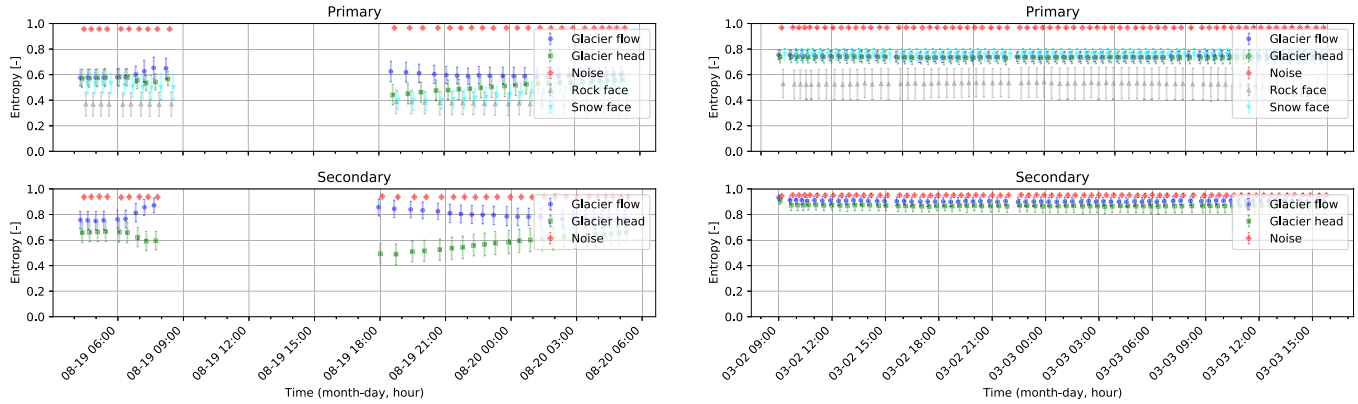

Fig. 9. Time series of entropy H for summer (left) and winter (right) seasons, for both monostatic (top) and bistatic (bottom) data, per ROI.

has an overall lower value in summer as opposed to winter, and exhibits intraday variation in summer, while remaining stable in winter.

In order to investigate possible occurrence of nonreciprocal scattering processes (i.e., processes where $S_{\mathrm{HV}} \neq S_{\mathrm{VH}}$) [17], [55], [94], Fig. 12 shows the time series of the relative values of the fourth eigenvalue of the coherency matrix λ_4 compared with the sum of all four eigenvalues, i.e., the plotted value is

$$\hat{\lambda}_4 = \frac{\lambda_4}{\sum_{n=1}^{4} \lambda_n}. \tag{20}$$

The data shows a low value of the $\hat{\lambda}_4$ in the monostatic datasets irrespective of the season. Bistatic datasets, however, show a higher value, thus indicating possible presence of nonreciprocal scattering.

C. Polarimetric Phase Differences

Polarimetric phase differences $\phi_{\mathrm{HH-VV}}$ and $\phi_{\mathrm{HV-VH}}$ can be used for investigation of anisotropy of the snow pack [11], as well as investigation of possible nonreciprocal scattering in the bistatic regime [55]. All phase differences shown in this section follow the sign convention described in Section II-F.

In order to assess the spatial and temporal behavior of the CPD $\phi_{\mathrm{HH-VV}}$, Figs. 13 and 14 show the maps of $\phi_{\mathrm{HH-VV}}$ for both devices and seasons, for the morning and evening time, respectively. The time series of $\phi_{\mathrm{HH-VV}}$ can be found in Fig. S6 of the Supplementary Material. Similarly to entropy and mean alpha angle, a large difference in behavior between seasons, and intraday variation in summer is observed.

The XPD $\phi_{\mathrm{HV-VH}}$ should have a zero value in the monostatic observations due to the reciprocity principle [50] (this is confirmed in Fig. S7 of the Supplementary Material), and thus, the bistatic behavior is of larger interest, as its nonzero value is an indicator of nonreciprocal scattering. Fig. 15 shows the maps of $\phi_{\mathrm{HV-VH}}$ for the secondary device in both seasons, for both the morning and evening time. The time series is shown in Fig. S8 of the Supplementary Material. The data confirms that $\phi_{\mathrm{HV-VH}}$ acquires a nonzero value in the bistatic regime, and the spatial and temporal behavior varies dramatically between the summer and the winter season.

IV. Discussion

A. Polarimetric Calibration and Limitations of the Dataset

Polarimetric calibration in the large-angle bistatic regime, where neither the reciprocity principle nor corner reflectors can be used, is usually more challenging than monostatic calibration [78]. The bistatic calibration in this experiment was performed with the VSPARC active calibrator [78], whereas the monostatic calibration was carried out using a combination of corner reflectors and the application of the reciprocity principle [93]. Table S-I shows the residuals of the polarimetric calibration of the primary device, however, these residuals are not available for the secondary device, since a second, independent validation target was not available. The observed data (e.g., bistatic alpha angle $\bar{\alpha}$) and a visual assessment of the Pauli basis scattering in Fig. 4 do suggest correctness of calibration, however, this limited validation has to be kept in mind when interpreting bistatic data.

Due to the processing complexity of polarimetric KAPRI data and topographic phase correction, care has to be taken that the shown polarimetric phase difference values in Figs. 13–15 are not just an artifact of inaccurate phase compensation. There are several indications that the observed phase differences are real. First, the shown XPD/CPD is relatively constant and no fringes—which are typically present when the topographic phase is incorrectly compensated—are observed. Second, the CPD observed in summer behaves similarly between the monostatic and bistatic dataset, starting with a strong offset in the morning and flattening in the evening. Finally, for the XPD, the VSPARC calibrator was placed near the "Glacier head" ROI in the summer acquisitions. It was set to the constant phase response configuration (described by [78, Eq. (39e)]), and thus, there was zero phase delay between VSPARC's signal in all polarimetric channels. Accordingly, in the bottom left map in Fig. 15 VSPARC can be seen as a point target exhibiting a zero XPD. There is, thus, a high degree of confidence that the XPD data in VSPARC's vicinity is correctly unwrapped and compensated. However, independent validation (preferably with a second crosspolarizing bistatic target placed in a second location) is desirable for future acquisitions to achieve certainty about the observed phase differences.

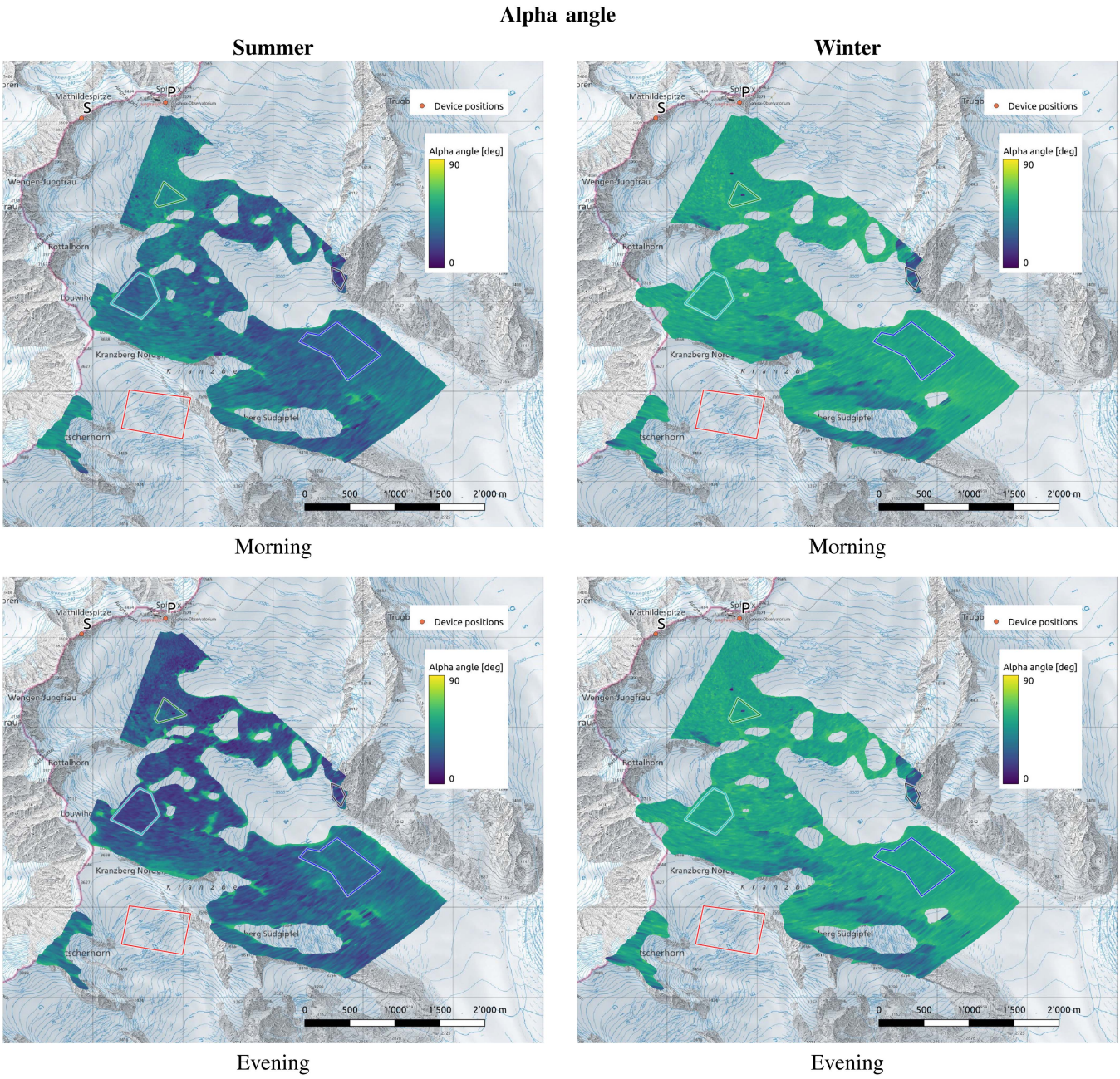

Fig. 10. Comparison of the observed monostatic mean alpha angle $\bar{\alpha}$ for the summer (left) and winter (right) seasons, for morning (top) and evening (bottom) times of day. In winter, $\bar{\alpha}$ retains a medium value throughout the day. In summer, $\bar{\alpha}$ is comparably lower. It also further reduces during the day and reaches its minimal value after sunset, in a manner similar to entropy in Fig. 8. The exception are exposed rock areas, which retain a low entropy value throughout.

The combined monostatic/bistatic setup allows us to investigate the behavior of observed polarimetric parameters as the bistatic angle changes from zero to a relatively high value of $50\,^{\circ}$. However, the geometry limitations do not allow sampling of a continuous β spectrum up to this maximal value. The sampling is instead limited only to the two ROIs within the bistatic beam ("Glacier head" and "Glacier flow"), with bistatic angle values of $40\,^{\circ}$ and $10\,^{\circ}$, respectively. Bistatic angles other than these values remain unavailable, and thus, the behavior cannot be easily generalized. Furthermore, the ground-based acquisition geometry also results in relatively shallow incidence angles of $75\,^{\circ}$ and $80\,^{\circ}$ in the two ROIs. The snow and rock face ROIs provide a relatively steep local incidence angle due to the mountainous geometry, however, are for the same reason more susceptible to foreshortening effects.

In this article, the entropy H and mean alpha angle α of the Cloude–Pottier incoherent target decomposition [17], [56] are analyzed in detail. Other parameters from decompositions, such as the roll-invariant incoherent target decomposition [57] (and, in the case of bistatic observations, its bistatic extension [58]) could potentially provide further detailed insights. However, due to limited spatial extent of the dataset, and thus, the inability to

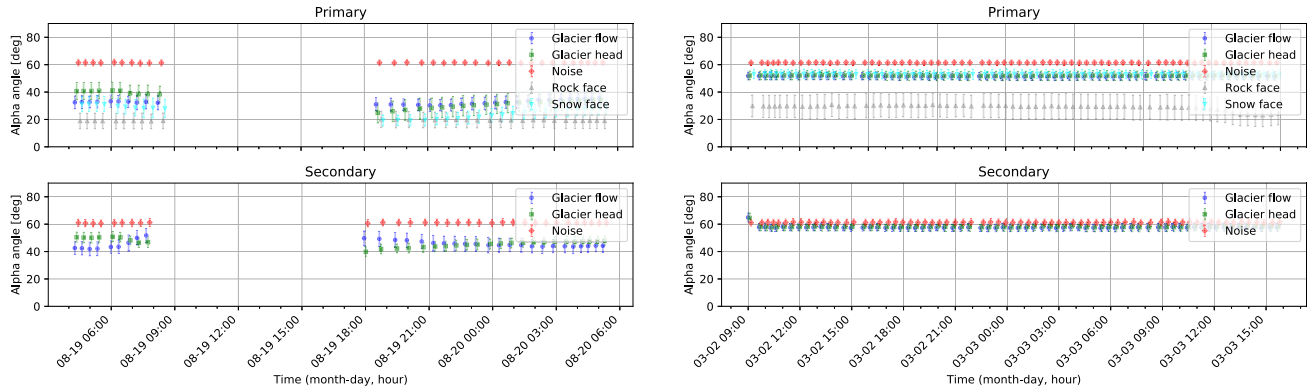

Fig. 11. Time series of mean alpha angle $\bar{\alpha}$ for summer (left) and winter (right) seasons, for both monostatic (top) and bistatic (bottom) data, per ROI.

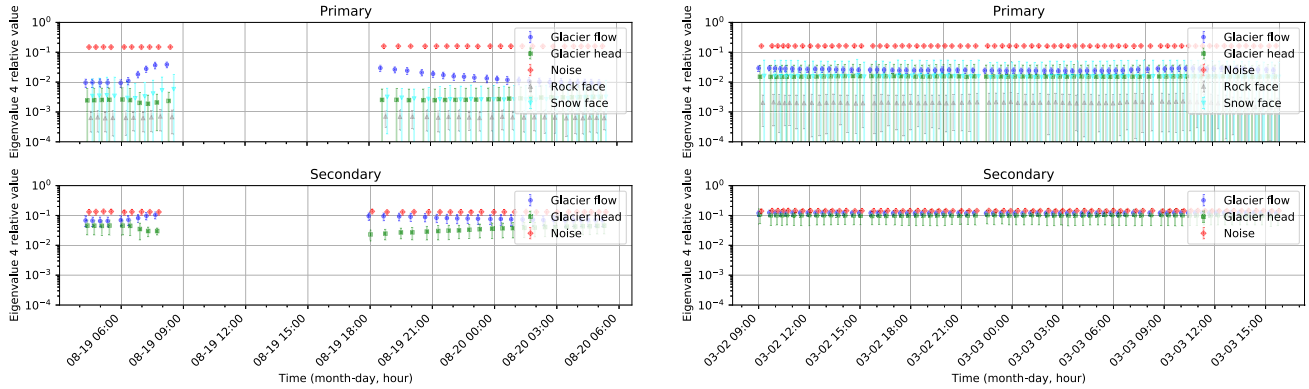

Fig. 12. Time series of the fourth eigenvalue $\hat{\lambda}_4$ as defined in (20) for summer (left) and winter (right) seasons, for both monostatic (top) and bistatic (bottom) data, per ROI. The y-axis is logarithmic. The primary (monostatic) datasets exhibit an overall low value irrespective of season or time of day. The temporal rise of $\hat{\lambda}_4$ value in the "Glacier flow" ROI in summer is correlated with the SNR reduction (see Fig. 5). The bistatic datasets (secondary) show a higher value of $\hat{\lambda}_4$, indicating presence of nonreciprocal scattering.

acquire sufficiently diverse and extensive statistics of different terrain types (especially after the necessary multilooking), such analysis is not carried out here.

B. Glacier Drift and Temporal Coherence

The estimated glacier drift shown in Fig. 6 and Table III is aligned with the results from a previous investigation using TanDEM-X data [21, Fig. 15], which determined the median horizontal glacier velocity of ~ 0.3 m/day in the "Glacier head" ROI, and ~ 0.2 m/day in the "Glacier flow" ROI. However, the ROIs lay within regions with low probability of velocity tracking success [21, Fig. 18], and thus, have to be interpreted with caution. For comparison, the global ice velocity dataset [98] yields mean velocity values of 0.17 m/day for "Glacier head" ROI and 0.24 m/day for "Glacier flow" ROI, thus, showing an opposite trend. This discrepancy (between our observations and the dataset in [98]) could have various causes, for example the 3-year gap between measurements, the difference in the temporal scale of the observations (days versus years), simplified geometric assumptions in Table III, uncompensated APSs, etc. However, the objective of the analysis of glacier drift in Section III-A is only to assess its magnitude for purpose of temporal decorrelation analysis as described in Section II-D1—for this a rough estimate of the drift value is sufficient. The values shown in Table III justify the decimation-based approach of Section II-D1, which mitigates the influence of drift on the observed coherence. We note that due to the temporal constraints of the dataset (measurements done only in four days of the year) and limited spatial coverage of the ROIs, the drift data shown in Table III can not be used to draw conclusions about the total mass balance of the glacier.

The temporal decay of coherence, shown in Fig. 7, indicates that coherence exhibits an exponential-like decay on the scale of hours during both seasons. In winter, the major contributing factor is likely small microstructural variations, which, even when small, have a considerable effect at short wavelengths, as temporal decorrelation occurs faster at short wavelength [63]. In summer, the "aged" snowpack can be possibly considered more stable in terms of microstructure, however, the considerable and periodic changes in liquid water content can contribute to rapid changes in scattering characteristics and, thus, cause decorrelation [99]. Since the start time T_0 was chosen in the evening, the snowpack was refreezing during the coherence monitoring window, and thus, there was no further loss of coherence due to reduction of SNR. However, the relatively low value of SNR

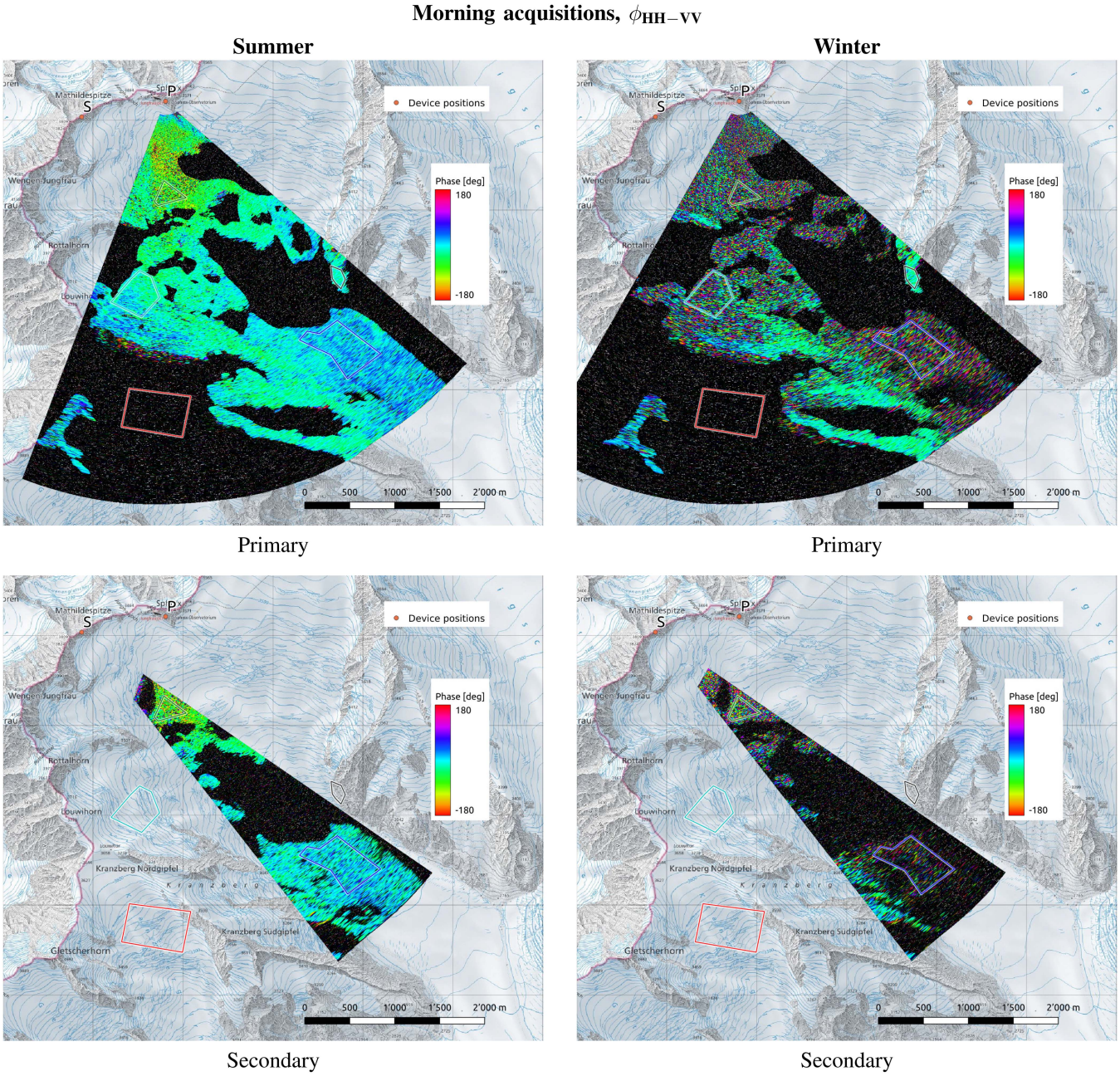

Fig. 13. Comparison of the observed CPD for the summer (left) and winter (right) seasons, for the primary (top, monostatic) and the secondary (bottom, bistatic) dataset. The data were acquired in the morning. In order to enhance the signal, ten consecutive interferograms were coherently averaged. In summer, the CPD has a "well-behaved" value, and does not appear to exhibit phase wrapping, neither in the monostatic nor the bistatic dataset. It exhibits an incidence angle dependent behavior, where its value increases with increasing incidence angle. In winter, the CPD considerably varies over very short spatial scales, and appears to exhibit phase wrapping. The exception are exposed rock areas, which retain a CPD value of close to 0.

can be a partial contributor to the low coherence estimate, especially in summer in the "Glacier flow" ROI, for which (15) and SNR values from Fig. 5 predict an SNR coherence loss factor $\gamma_{\text{SNR}} \approx 0.9$.

The characteristic decorrelation timescale (i.e., the timescale on which coherence reduces to $1/e \approx 0.36$) can be estimated as $4-8$ h in summer, and $6-12$ h in winter. This has strong implications for repeat-pass interferometric methods–applying repeat-pass interferometric methods with temporal baselines longer than a few hours may not be feasible due to almost complete decorrelation of the snowpack. Spaceborne SAR missions are particularly affected, since their revisit times usually have a value on scale of several days. Spaceborne Ku-band SAR missions might thus not be able to apply repeat-pass interferometric methods over snow-covered areas, unless steps are taken to reduce this temporal baseline, e.g., through use of constellations.

It should be noted that in some experiments under different conditions and in different observation areas, the decorrelation time of snow cover at Ku-band was observed to be

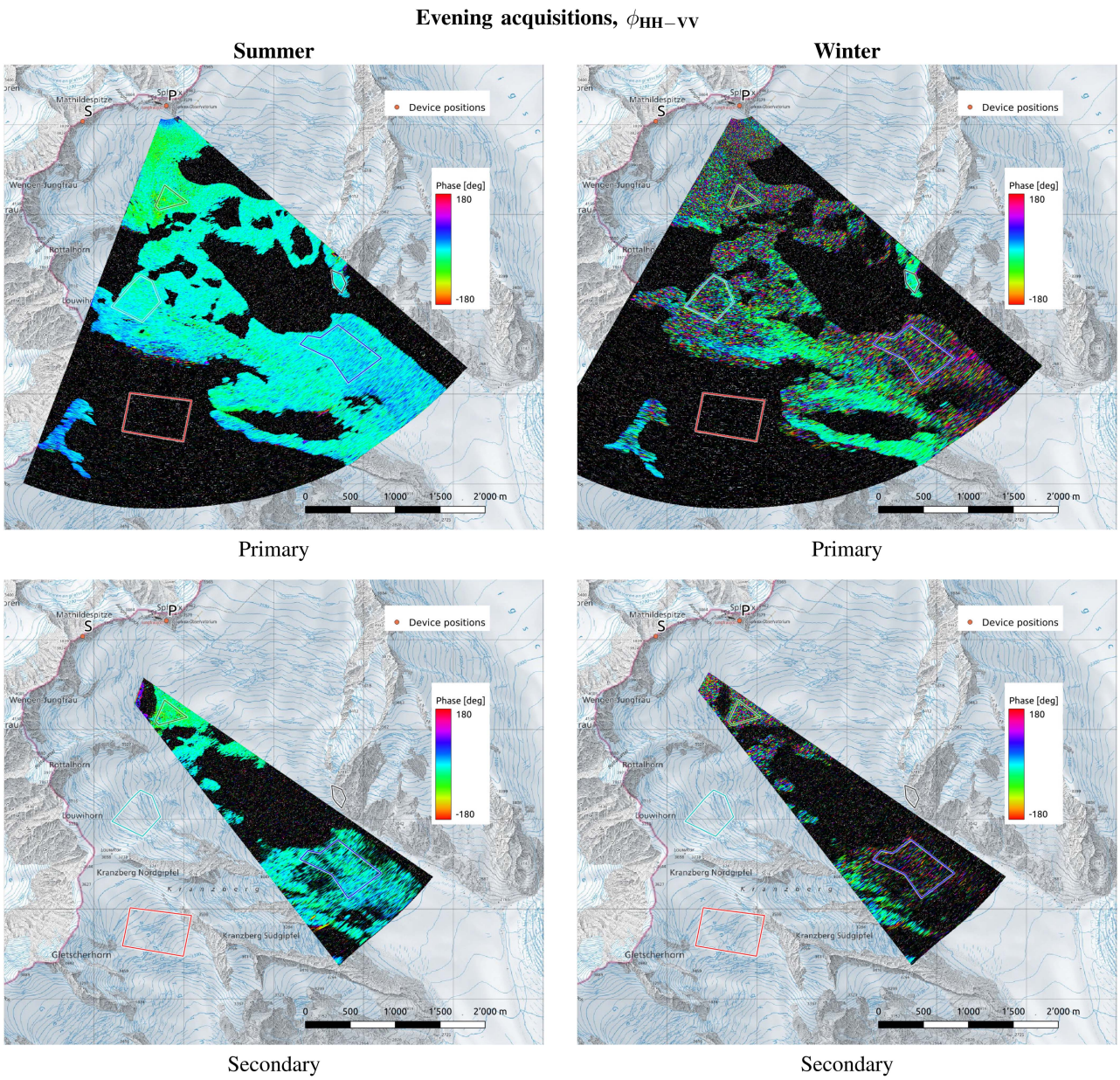

Fig. 14. Comparison of the observed CPD for the summer (left) and winter (right) seasons, for the primary (top, monostatic) and the secondary (bottom, bistatic) dataset. The acquisitions were taken in the evening. In order to enhance the signal, ten consecutive interferograms were coherently averaged. Compared with the morning acquisitions (Fig. 13), the phase gradient in summer has flattened and the values are closer to zero throughout the scene. In winter, the high rate of spatial variation of CPD remains throughout the day.

longer—for example, data in [74] shows sustained coherence between Ku-band tomograms of snow cover over baselines up to 14 h.

The coherence decay observed in [62] at similar wavelengths (16.8 GHz) shows a similar trend to our observations during snow melt, i.e., rapid decay of coherence on the order of hours. However, during the presence of dry snow, in [62] a much lower typical rate of coherence decay was observed, with the snowpack remaining partially coherent ($\gamma \approx 0.5$) for several tens of days. A possible explanation for this discrepancy may be the difference in observation sites and meteorological conditions—our observations were carried out on a high-altitude glacier, with strong wind gusts up to 45 km/h (see Fig. S2 of the Supplementary Material). Indeed, in [62], similarly rapid coherence decay was observed during a period of similarly strong wind, which followed after fresh snowfall. Furthermore, the snow depths in our study (2–4 m in winter) are much deeper than in [62] where snow depth ranged typically between 20 cm and 80 cm. It could thus be expected that ground signal contributes more considerably to the backscatter in [62] and keeps the coherence high, whereas the snow volume contributes more in our study, and thus, exhibits a higher decorrelation rate due to snow redistribution.

Nevertheless, comparison with the previous studies [62], [74] indicates that our observed rates of decorrelation can not be simply extrapolated to all snow-covered environments, and

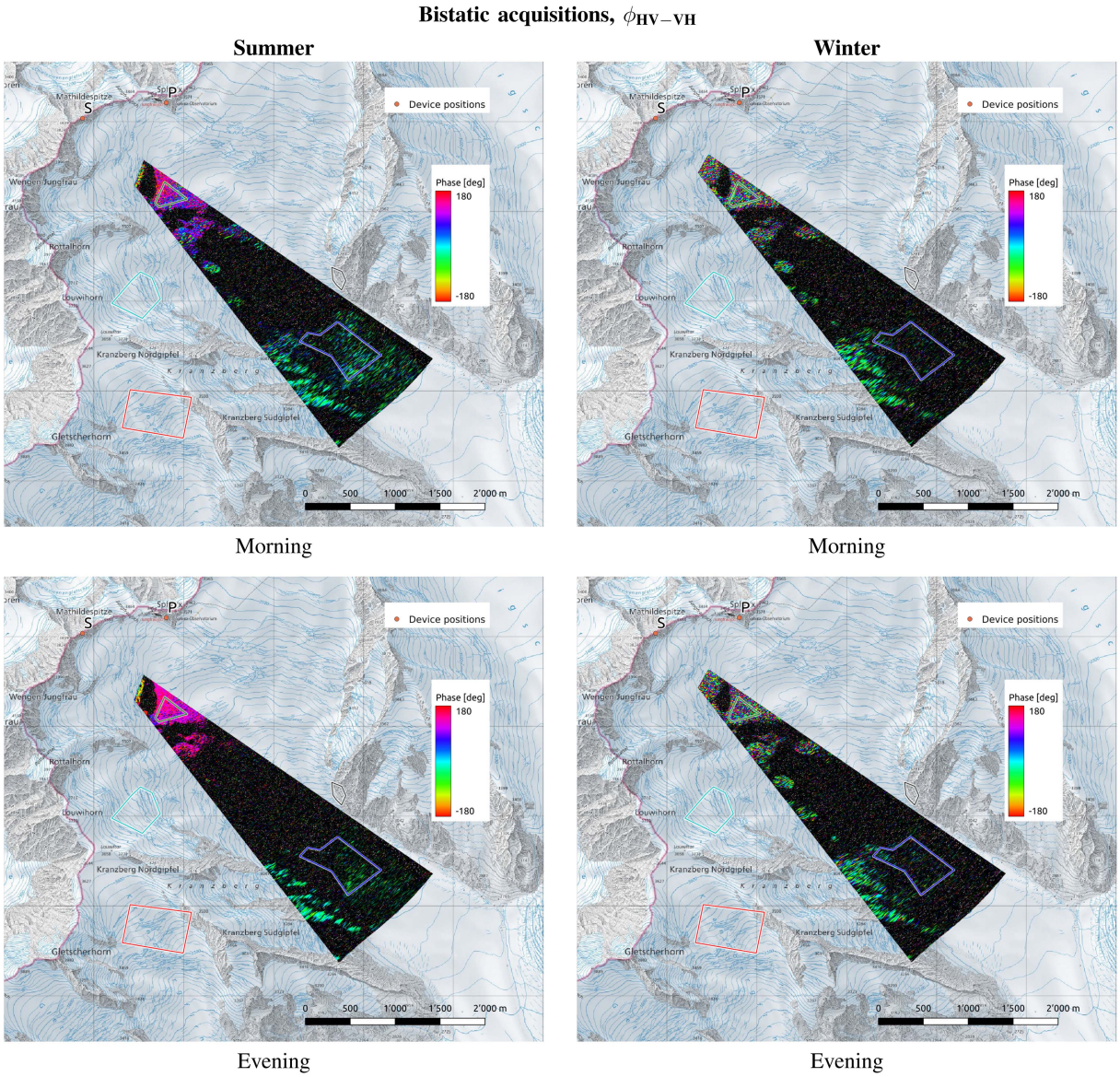

Fig. 15. Comparison of the XPD observed by the secondary (bistatic) device, for the summer (left) and winter (right) seasons, for morning (top) and evening (bottom) acquisition time, respectively. In order to enhance the signal, ten consecutive interferograms were coherently averaged. For both seasons, the bistatic acquisitions show significant deviations from this zero value throughout the scene. In summer, in the near range at steeper incidence angles and large bistatic angle the XPD has a large value near 180°. With increasing range and incidence angle (and decreasing bistatic angle), this value appears to reduce toward zero, however, precise interpretation is difficult due to low coverage of medium bistatic angles. In the evening, the bistatic XPD in summer has a smoother behavior, however, the strong deviation from the zero value remains. In winter, the XPD exhibits similar behavior to CPD, varying considerably on short spatial scales. Even with 10× coherent averaging, the bistatic dataset exhibits very low SNR in the far range.

possibly also not to all times of year in the same environment. Further study is thus needed in order to determine whether the observed rates of decorrelation are also representative for other meteorological conditions and environments.

C. Second-Order Polarimetric Parameters

1) Entropy: The time series of entropy (Fig. 9) follows an expected trend in all datasets—the polarimetric entropy is high in winter and constant over time, which suggests a large diversity of scattering processes. In summer, the entropy is lower overall, and also exhibits a variation over the course of the day. This suggests that deterministic scattering processes, such as surface scattering, have a higher proportion, which is in agreement with the interpretation that melt-freeze crusts are present close to the surface in summer and cause a contribution of low-entropy surface scattering [17]. Furthermore, the temporal variation indicates that entropy reduces further as snow melt sets in during daytime, which increases liquid water content and reduces penetration depth [46], resulting in even larger contribution of surface scattering to total observed backscatter. The only exception is the behavior of "Glacier flow" ROI in the bistatic dataset in summer, where the rise in entropy with increasing snow melt can be explained as loss of signal, i.e., the entropy is calculated mostly on noise, which has very high intrinsic entropy.

2) Mean Alpha Angle: The mean alpha angle $\bar{\alpha}$ (Fig. 11) exhibits behavior very similar to entropy, and can be explained with the same interpretation. The value of $\bar{\alpha}$ between 40° and 60° is in agreement with dominance of volume scattering in winter. Lower values in summer suggest a larger (relative) contribution of surface scattering, and the temporal behavior is in agreement with increasing contribution of surface scattering due to increased liquid water content, with the "Glacier flow" ROI in the secondary dataset once again exhibiting an exceptional increase due to loss of SNR.

3) Fourth Eigenvalue λ_4: The fourth eigenvalue λ_4 of the coherency matrix T should have a zero value in the monostatic case due to the reciprocity principle [94]. This is confirmed in Fig. 12 which shows that the estimate of the value of $\hat{\lambda}_4$ does not exceed 0.03, with the exception of the evening of the summer period, where noise becomes a considerable factor. The slightly higher estimates in winter can be caused by a higher diversity of cross-polarizing scattering processes, which could "leak" into the fourth Pauli component, and thus, into the fourth eigenvalue. The effect in the monostatic dataset is, however, very limited and the absolute value remains low.

In the bistatic case, $\hat{\lambda}_4$ is higher overall—this can be due to several contributing factors. First, the SNR is overall lower in the bistatic case, which could cause an increase in the estimate of $\hat{\lambda}_4$. However, the comparison of monostatic summer SNR in "Glacier flow" ROI with the bistatic SNR in "Glacier head" ROI indicates that the bistatic data should have sufficient SNR. The second contributing factor could be a higher diversity of cross-polarizing scattering processes, just like in the monostatic winter data. This, however, does not completely explain why the value is also high in summer, where cross-polarizing contributions are quite low. The third possible factor is miscalibration, which could cause a contribution in case the amplitudes or phases of cross-polarized channels are not precisely calibrated. This effect certainly can not be excluded, due to factors mentioned in Section IV-A. However, miscalibration likely is not the only factor, since the higher values of $\hat{\lambda}_4$ are detected in both seasons, which were calibrated separately, and $\hat{\lambda}_4$ also exhibits a slight temporal trend in the "Glacier head" ROI, which indicates that it is caused by a true scattering signal. Furthermore, the XPD maps shown in Fig. 15 (and timeseries in Fig. S8 of the Supplementary Material) indicate that there are nonreciprocal scattering processes occurring in the scene, which will then result in nonzero value of the fourth Pauli component $k_{\mathrm{P4}} = j/\sqrt{2}(S_{\mathrm{HV}} - S_{\mathrm{VH}})$, and nonzero fourth eigenvalue of the T matrix. The nonzero value of $\hat{\lambda}_4$ is, thus, most likely caused by the same nonreciprocal processes that cause the nonzero XPD, and the quantification of $\hat{\lambda}_4$ in Fig. 12 can be used as an estimate of the contribution of these processes to total backscatter.

D. Polarimetric Phase Differences

1) Co-Polar Phase Difference: The CPD $\phi_{\mathrm{HH-VV}}$ (Figs. 13 and 14) exhibits a similar behavior between monostatic and bistatic datasets. In summer, it exhibits an incidence angle dependence, which varies with time of the day. When the snow cover is frozen (i.e., in the morning), $\phi_{\mathrm{HH-VV}}$ has a strong negative value at low incidence angles (near range), and trends toward a slight positive value at high incidence angles (far range), for both the monostatic and the bistatic dataset. It is difficult to interpret the change of the sign of CPD between these two areas as an effect caused purely by birefringence, since it would require a large change in the snow cover's structure and anisotropy between the two observed regions. An alternative interpretation of the change of the sign of CPD could be a change in the relative contribution of dihedral (double-bounce) scattering between the two geometries, where the contribution is larger at lower local incidence angles (i.e., near range). Fig. 4, acquired in the morning, shows a more dominant red color in the near-range region in summer, indicating a higher contribution of dihedral scattering. Dihedral scattering contribution has opposing effects on phases of the HH and VV channels (increasing the phase of one and decreasing the phase of the other, all else being equal) [17], and thus, could cause a sign flip of $\phi_{\mathrm{HH-VV}}$ if the relative contribution of double-bounce scattering to total backscatter changes.

This observed spatial trend of $\phi_{\mathrm{HH-VV}}$ in summer can be compared with literature. The incidence angle dependence has the opposite trend to values observed at X-band in Greenland [31, Figs. 3–5] and L-band in Svalbard [100, Figs. 8 and 9], where the $\phi_{\mathrm{HH-VV}}$ phase difference showed divergence from the zero value with increasing range. In SnowScat observations of fresh snow at Ku-band [11, Fig. 6] (note that the values in the referenced figure show $\phi_{\mathrm{VV-HH}}$), the $\phi_{\mathrm{HH-VV}}$ value was observed to be increasingly negative with increasing incidence angle, also a trend opposite to our observations. It should be noted, however, that the snow and observation conditions in these mentioned publications greatly differed from the setup and conditions of our observations, since our observations in summer were observing aged seasonal snow cover, which has repeatedly melted and refrozen over the course of the preceding season. Determination of the precise cause of the observed CPD behavior remains an open question, which certainly warrants further quantitative analysis.

Temporally, the summer CPD observations show that as liquid water content increases throughout the day, for all ROIs the phase difference shifts toward zero. This is in agreement with the interpretation that liquid water reduces penetration, and thus, the scattering behavior becomes more surface-like. Afterward, overnight when the snow cover refreezes, the CPD recovers toward its original value. A similar trend was observed in melting and refreezing snow at 95 GHz in [96, Fig. 7], where the accumulation of fresh snow cover observed under a 60° incidence angle caused a strong negative value of $\phi_{\mathrm{HH-VV}}$, which quickly reverted toward zero once the snow cover started melting.

In winter, a high rate of spatial variation of the CPD is observed, which can be attributed to a high contribution of volume scattering [48], together with a range cell size orders of magnitude larger than the wavelength, causing the positions of the HH and VV phase centers to vary on scales longer than the wavelength. Only the exposed rock face maintains the zero value of CPD, as expected for surface-type scattering. This has implications for scattering models, which might aim to invert the CPD for estimates of structural anisotropy or depth—this approach is often applied at longer wavelengths [11], [13]. However, due to the short Ku-band wavelength, even small

values and variations of anisotropy or relatively short depths can cause sufficient phase delay between the two polarizations so as to cause phase wrapping. We confirmed this by an exploratory analysis of the model presented in [13], which relates the CPD to snow grain shape anisotropy—it has shown that at the Ku-band, with a density fraction value of 0.3 and snow depth of 3 m even small variation of any input model parameter causes considerable CPD change and phase wrapping. This is corroborated by the observed winter data, which shows a high rate of spatial variation of CPD even in areas which otherwise appear uniform both visually and in terms of observed backscatter intensity. This variation and phase wrapping makes simple parameter inversion challenging since there is no bijective function between CPD and model parameter values.

However, while the CPD in winter might appear to behave like noise spatially, it remains temporally stable for any particular point on scales of minutes to hours. Thus, by monitoring the CPD with a sufficient temporal resolution, one can monitor this CPD evolution and possibly derive information about the temporal influence of parameters that affect the CPD, such as redistribution and settling of snowpack. This temporal evolution could be particularly interesting to observe just after fresh snowfall—this did unfortunately not occur during our observation windows, but is an observation scenario of interest for future investigations.

2) Cross-Polar Phase Difference: The XPD $\phi_{\mathrm{HV-VH}}$ confirms the validity of the reciprocity principle ($S_{\mathrm{HV}} = S_{\mathrm{VH}}$), as all monostatic datasets (see Fig. S7 of the Supplementary Material) exhibit a zero value of $\phi_{\mathrm{HV-VH}}$, regardless of the scattering medium. However, it exhibits a very interesting behavior in the bistatic datasets (Fig. 15). In winter, it varies considerably on short spatial scales, similarly to the CPD. This can also be interpreted as a large contribution of volume scattering, which causes a large variation of the HV and VH phase center positions.

In summer, a large positive value of $\phi_{\mathrm{HV-VH}}$ (approx. $+150\,^{\circ}$) is observed in the "Glacier head" ROI. This value appears to further increase with increase of liquid water content due to snowmelt. In the far range (and low bistatic angles), the XPD appears to trend toward the zero value, however, the SNR is relatively weak due to the long range, use of low gain antennas, and absorption by liquid water.

One interpretation of the nonzero XPD value can be proposed as a combination of snow birefringence (which also causes the CPD [11]) and a geometric effect caused by the difference between local incidence angles of the transmission and reception legs of the scattered signal (i.e., a different local incidence angle from the point of view of the primary and of the secondary device). This can cause a different phase delay contribution of the two journey segments (the primary-to-scatterer segment and the scatterer-to-secondary segment), which thus do not cancel each other out between the HV and VH channels as they would when monostatic observations are made—Fig. 16 visualizes this interpretation. To the best of the authors' knowledge, there are no similar observations of snow cover at large bistatic angles at radio frequencies available in literature to date, and thus, no comparisons with results from other observations can be made. The definitive identification of the mechanism causing the nonzero XPD value remains an open question, which certainly invites further investigation.

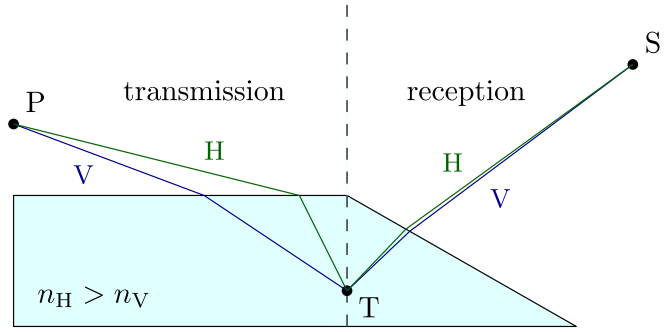

Fig. 16. Possible interpretation of non-zero $\phi_{\mathrm{HV-VH}}$ value caused by combination of birefringence of the snow pack (i.e., difference in refractive indices n_{H} and n_{V}) and difference in incidence angles of the transmission and reception legs of the signal's path. The transmission leg causes a significant difference between the phase delays of the H- and V- polarized waves. The reception leg then causes a much smaller difference in the opposite direction, thus the combined VH pathway accumulates a longer phase delay than the HV pathway, resulting in positive value of $\phi_{\mathrm{HV-VH}}$. In the monostatic case (where both transmission and reception paths occur on the left side of this diagram), the phase differential accumulated during the transmission leg is cancelled out by the reversed differential during the reception leg.

Regardless of the cause, both the summer and the winter observations show that nonreciprocal backscatter does occur in snow cover at nonzero bistatic angles, and thus, care has to be taken not to automatically assume reciprocity during calibration/analysis of bistatic radar backscatter over snow-covered regions.

V. Conclusion

In this publication we presented the first application of a long-baseline bistatic KAPRI radar setup to monitoring of natural environments. To the best of the authors' knowledge, this dataset, acquired on top of the Jungfraufirn region of the Great Aletsch Glacier, provides the first polarimetric characterization of Ku-band backscatter from snow-covered areas at nonnegligible bistatic angles on range scales of kilometers. The observations revealed high variability of polarimetric properties of backscatter from the observed snow cover between the late summer and late winter seasons, and in some cases also variability between the monostatic and bistatic backscatter, as well as temporal variability in summer.

We observed that temporal decorrelation of snow cover in the observed area at Ku-band occurs on timescales of hours, with coherence reducing to $1/e$ within time durations between 4 and 12 h. While this value might be different in other times of year and areas, the timescale of hours provides an order-of-magnitude estimate of the upper limit imposed on the revisit time of repeat-pass methods, such as differential interferometry or SAR tomography. The limit on the scale of hours (or lower tens of hours) will make using these methods with spaceborne Ku-band systems extremely challenging, since spaceborne systems usually have revisit times on the order of days.

The second-order polarimetric parameters, the entropy H and the mean alpha angle $\bar{\alpha}$, exhibit an expected trend of a lower

value in summer when the snow cover has aged and liquid water content causes dominance of surface scattering, and a higher value in winter when fresh snow allows deep penetration and occurrence of a higher diversity of scattering processes.

The polarization phase differences $\phi_{\mathrm{HH-VV}}$ and $\phi_{\mathrm{HV-VH}}$ show a very interesting behavior, both between the two seasons, and between monostatic and bistatic acquisitions. The CPD in winter varies considerably on short spatial scales, which confirms that CPD-based inversion methods are challenging to apply at Ku-band due to the phase-wrapping tendency when observing snow layers thicker than several tens of centimeters. In summer, it exhibits a smooth incidence-angle-dependent trend, and its value also exhibits an intraday cycle, which can likely be attributed to changes in liquid water content of the snow cover. The XPD exhibits an expected zero value in all monostatic datasets (as seen in Fig. S7 of the Supplementary Material); however, in the bistatic datasets, there is a substantial deviation from this zero value. This indicates the presence of nonreciprocal scattering behaviors at nonzero bistatic angles in snow, which has implications both for snow modeling using bistatic data, as well as polarimetric calibration procedures, which can no longer rely on the reciprocity principle.

Besides the above-mentioned information about behavior of polarimetric parameters at Ku-band, lessons learned from the two observation campaigns also suggest attractive future observation targets, such as the observation of the minute-scale temporal behavior of polarization phase differences during and immediately after fresh snowfall, as well as long-term monitoring of the transition from fresh winter snow to refrozen summer snow. The presented data can also already serve as a reference overview for polarimetric Ku-band scattering behavior of snow under a variety of conditions, which can aid planning and development of airborne and spaceborne missions operating at similar wavelengths.

Acknowledgment

The authors would like to thank the International Foundation High Altitude Research Stations Jungfraujoch and Gornergrat (HFSJG), 3012 Bern, Switzerland, for enabling us to carry out our experiments at the Jungfraujoch High Altitude Research Station. The authors would also like to thank the custodians Daniela Bissig, Erich Furrer, and Christine and Ruedi Käser for the support of our activities, Michael Arnold, Jorit Schmelzle, and Pol Villalvilla for their invaluable support during campaigns, and Silvan Leinss and Charles Werner for their technical support regarding radar operation. They would like to thank Marc Rodriguez-Cassola, Keith Morrison, Jordi Mallorqui, and four anonymous reviewers for their feedback on the manuscript. Map underlay: Landeskarte 1:25000, Federal Office of Topography swisstopo.

References

[1] A. W. Nolin, "Recent advances in remote sensing of seasonal snow," *J. Glaciol.*, vol. 56, no. 200, pp. 1141–1150, 2010.

[2] J. King et al., "Spatio-temporal influence of tundra snow properties on Ku-band (17.2 GHz) backscatter," *J. Glaciol.*, vol. 61, no. 226, pp. 267–279, 2015.

[3] J. Lemmetyinen et al., "Nordic snow radar experiment," *Geosci. Instrum., Methods Data Syst.*, vol. 5, no. 2, pp. 403–415, 2016.

[4] L. Tsang et al., "Review article: Global monitoring of snow water equivalent using high frequency radar remote sensing," *Cryosphere Discuss.*, vol. 2021, pp. 1–57, 2021. [Online]. Available: https://tc.copernicus.org/preprints/tc-2021-295/

[5] A. Thompson, R. Kelly, and J. King, "Sensitivity of Ku- and X-band radar observations to seasonal snow in Ontario, Canada," *Can. J. Remote Sens.*, vol. 45, no. 6, pp. 829–846, 2019, doi: 10.1080/07038992.2019.1704621.

[6] J. Shi and J. Dozier, "Mapping seasonal snow with SIR-C/X-SAR in mountainous areas," *Remote Sens. Environ.*, vol. 59, no. 2, pp. 294–307, 1997. [Online]. Available: https://www.sciencedirect.com/science/article/pii/S0034425796001460

[7] N. Rutter et al., "Effect of snow microstructure variability on Ku-band radar snow water equivalent retrievals," *Cryosphere*, vol. 13, no. 11, pp. 3045–3059, 2019. [Online]. Available: https://tc.copernicus.org/articles/13/3045/2019/

[8] C. Derksen et al., "A dual-frequency Ku-band radar mission concept for seasonal snow," in *Proc. IEEE Int. Geosci. Remote Sens. Symp.*, 2019, pp. 5742–5744.

[9] A. Wiesmann, C. Mätzler, and T. Weise, "Radiometric and structural measurements of snow samples," *Radio Sci.*, vol. 33, no. 2, pp. 273–289, Mar. 1998, doi: 10.1029/97RS02746.

[10] J. Lemmetyinen et al., "Simulating seasonally and spatially varying snow cover brightness temperature using HUT snow emission model and retrieval of a microwave effective grain size," *Remote Sens. Environ.*, vol. 156, pp. 71–95, 2015, doi: 10.1016/j.rse.2014.09.016. [Online]. Available: https://www.sciencedirect.com/science/article/pii/S0034425714003605

[11] S. Leinss, H. Löwe, M. Proksch, J. Lemmetyinen, A. Wiesmann, and I. Hajnsek, "Anisotropy of seasonal snow measured by polarimetric phase differences in radar time series," *Cryosphere*, vol. 10, no. 4, pp. 1771–1797, 2016.

[12] N. M. Rathmann, D. A. Lilien, A. Grinsted, T. A. Gerber, T. J. Young, and D. D. Jensen, "On the limitations of using polarimetric radar sounding to infer the crystal orientation fabric of ice masses," *Geophys. Res. Lett.*, vol. 49, no. 1, 2022, Art. no. e2021GL096244.

[13] G. Parrella, I. Hajnsek, and K. P. Papathanassiou, "Retrieval of Firn thickness by means of polarisation phase differences in L-band SAR data," *Remote Sens.*, vol. 13, no. 21, 2021, Art. no. 4448. [Online]. Available: https://www.mdpi.com/2072-4292/13/21/4448

[14] H. Rott et al., "CoReH2O, A dual frequency radar mission for snow and ice observations," in *Proc. IEEE Int. Geosci. Remote Sens. Symp.*, 2012, pp. 5550–5553.

[15] National Research Council, *Earth Science and Applications From Space: National Imperatives for the Next Decade and Beyond*. Washington, DC, USA: Nat. Academies Press, 2007. [Online]. Available: https://nap.nationalacademies.org/catalog/11820/earth-science-and-applications-from-space-national-imperatives-for-the

[16] C. Derksen et al., "Development of the terrestrial snow mass mission," in *Proc. IEEE Int. Geosci. Remote Sens. Symp.*, 2021, pp. 614–617.

[17] J.-S. Lee and E. Pottier, *Polarimetric Radar Imaging: From Basics to Applications*. Boca Raton, FL, USA: CRC Press, 2009.

[18] A.-L. Germond, E. Pottier, and J. Saillard, "Foundations of bistatic radar polarimetry theory," in *Proc. Radar (Conf. Publ. No 449)*, 1997, pp. 833–837.

[19] G. Krieger et al., "TanDEM-X: A satellite formation for high-resolution SAR interferometry," *IEEE Trans. Geosci. Remote Sens.*, vol. 45, no. 11, pp. 3317–3341, Nov. 2007.

[20] P. Rizzoli, M. Martone, H. Rott, and A. Moreira, "Characterization of snow facies on the Greenland ice sheet observed by TanDEM-X interferometric SAR data," *Remote Sens.*, vol. 9, no. 4, 2017, Art. no. 315. [Online]. Available: https://www.mdpi.com/2072-4292/9/4/315

[21] S. Leinss and P. Bernhard, "TanDEM-X:Deriving InSAR height changes and velocity dynamics of great Aletsch glacier," *IEEE J. Sel. Topics Appl. Earth Observ. Remote Sens.*, vol. 14, pp. 4798–4815, May 2021.

[22] M. Stefko, S. Leinss, O. Frey, and I. Hajnsek, "Coherent backscatter enhancement in bistatic Ku- and X-band radar observations of dry snow," *Cryosphere*, vol. 16, no. 7, pp. 2859–2879, 2022. [Online]. Available: https://tc.copernicus.org/articles/16/2859/2022/

[23] P. L. Dekker, H. Rott, P. P. Iraola, B. Chapron, K. Scipal, and E. D. Witte, "Harmony: An Earth Explorer 10 Mission candidate to observe land, ice, and ocean surface dynamics," in *Proc. IEEE Int. Geosci. Remote Sens. Symp.*, 2019, pp. 8381–8384.

[24] A. Moccia, G. Rufino, M. D'Errico, G. Alberti, and G. Salzillo, "BISSAT: A bistatic SAR for Earth observation," in *Proc. Int. Geosci. Remote Sens. Symp.*, 2002, vol. 5, pp. 2628–2630.

[25] D. Massonnet, "The interferometric cartwheel: A constellation of passive satellites to produce radar images to be coherently combined," *Int. J. Remote Sens.*, vol. 22, no. 12, pp. 2413–2430, Jan. 2001. [Online]. Available: https://www.tandfonline.com/doi/full/10.1080/01431160118952

[26] H. A. Zebker, T. G. Farr, R. P. Salazar, and T. H. Dixon, "Mapping the world's topography using radar interferometry: The TOPSAT mission," *Proc. IEEE*, vol. 82, no. 12, pp. 1774–1786, Dec. 1994.

[27] N. Gebert, B. C. Dominguez, M. W. J. Davidson, M. D. Martin, and P. Silvestrin, "SAOCOM-CS - A passive companion to SAOCOM for single-pass l-band SAR interferometry," in *Proc. 10th Eur. Conf. Synthetic Aperture Radar*, 2014, pp. 1–4.

[28] S. Tan, W. Chang, L. Tsang, J. Lemmetyinen, and M. Proksch, "Modeling both active and passive microwave remote sensing of snow using dense media radiative transfer (DMRT) theory with multiple scattering and backscattering enhancement," *IEEE J. Sel. Topics Appl. Earth Observ. Remote Sens.*, vol. 8, no. 9, pp. 4418–4430, Sep. 2015.

[29] A. Wiesmann and C. Mätzler, "Microwave emission model of layered snowpacks," *Remote Sens. Environ.*, vol. 70, no. 3, pp. 307–316, 1999.

[30] A. Rees, J. Lemmetyinen, C. Derksen, J. Pulliainen, and M. English, "Observed and modelled effects of ice lens formation on passive microwave brightness temperatures over snow covered tundra," *Remote Sens. Environ.*, vol. 114, no. 1, pp. 116–126, 2010.

[31] G. Parrella, I. Hajnsek, and K. P. Papathanassiou, "Model-based interpretation of PolSAR data for the characterization of glacier zones in Greenland," *IEEE J. Sel. Topics Appl. Earth Observ. Remote Sens.*, vol. 14, pp. 11 593–11 607, Nov. 2021.

[32] A. Wiesmann et al., "SnowScat, X-to Ku-band scatterometer development," in *Proc. ESA Living Planet Symp.*, 2010, vol. 686, Art. no. 160.

[33] J. Dozier and J. Shi, "Estimation of snow water equivalence using SIR-C/X-SAR. I. inferring snow density and subsurface properties," *IEEE Trans. Geosci. Remote Sens.*, vol. 38, no. 6, pp. 2465–2474, Nov. 2000.

[34] A. Patil, G. Singh, C. Rudiger, S. Mohanty, S. Kumar, and Snehmani, "A novel approach for the snow water equivalent retrieval using x-band polarimetric synthetic aperture radar data," *IEEE Trans. Geosci. Remote Sens.*, vol. 59, no. 5, pp. 3753–3763, May 2021.

[35] S. Manickam, A. Bhattacharya, G. Singh, and Y. Yamaguchi, "Estimation of snow surface dielectric constant from polarimetric SAR data," *IEEE J. Sel. Topics Appl. Earth Observ. Remote Sens.*, vol. 10, no. 1, pp. 211–218, Jan. 2017.

[36] M. Surendar, A. Bhattacharya, G. Singh, and G. Venkataraman, "Estimation of snow density using full-polarimetric synthetic aperture radar (SAR) data," *Phys. Chem. Earth*, vol. 83/84, pp. 156–165, 2015.

[37] X. Xu, L. Tsang, and S. Yueh, "Electromagnetic models of co/cross polarization of bicontinuous/DMRT in radar remote sensing of terrestrial snow at X- and Ku-band for CoReH2O and SCLP applications," *IEEE J. Sel. Topics Appl. Earth Observ. Remote Sens.*, vol. 5, no. 3, pp. 1024–1032, Jun. 2012. [Online]. Available: http://doi.wiley.com/10.1029/97RS02746

[38] W. Chang, K. H. Ding, L. Tsang, and X. Xu, "Microwave scattering and medium characterization for terrestrial snow with QCA-Mie and bicontinuous models: Comparison studies," *IEEE Trans. Geosci. Remote Sens.*, vol. 54, no. 6, pp. 3637–3648, Jun. 2016.

[39] A. Muhuri, S. Manickam, A. Bhattacharya, and Snehmani, "Snow cover mapping using polarization fraction variation with temporal radarsat-2 C-band full-polarimetric SAR data over the Indian Himalayas," *IEEE J. Sel. Topics Appl. Earth Observ. Remote Sens.*, vol. 11, no. 7, pp. 2192–2209, Jul. 2018.

[40] T. Jagdhuber, J. Stockamp, I. Hajnsek, and R. Ludwig, "Identification of soil freezing and thawing states using SAR polarimetry at C-band," *Remote Sens.*, vol. 6, pp. 2008–2023, 2014.

[41] A. Muhuri, S. Manickam, and A. Bhattacharya, "Scattering mechanism based snow cover mapping using Radarsat-2 C-band polarimetric SAR data," *IEEE J. Sel. Topics Appl. Earth Observ. Remote Sens.*, vol. 10, no. 7, pp. 3213–3224, Jul. 2017.

[42] Y. L. S. Tsai, A. Dietz, N. Oppelt, and C. Kuenzer, "Remote sensing of snow cover using spaceborne SAR: A review," *Remote Sens.*, vol. 11, no. 12, 2019, Art. no. 1456.

[43] Snehmani, M. K. Singh, R. D. Gupta, A. Bhardwaj, and P. K. Joshi, "Remote sensing of mountain snow using active microwave sensors: A review," *Geocarto Int.*, vol. 30, no. 1, pp. 1–27, 2015, doi: 10.1080/10106049.2014.883434.

[44] S. Awasthi and D. Varade, "Recent advances in the remote sensing of alpine snow: A review," *GISci. Remote Sens.*, vol. 58, no. 6, pp. 852–888, 2021, doi: 10.1080/15481603.2021.1946938.

[45] A. J. Dietz, C. Kuenzer, U. Gessner, and S. Dech, "Remote sensing of snow–A review of available methods," *Int. J. Remote Sens.*, vol. 33, no. 13, pp. 4094–4134, 2012, doi: 10.1080/01431161.2011.640964.

[46] C. Mätzler, "Applications of the interaction of microwaves with the natural snow cover," *Remote Sens. Rev.*, vol. 2, no. 2, pp. 259–387, 1987, doi: 10.1080/02757258709532086.

[47] O. Frey, C. L. Werner, R. Caduff, and A. Wiesmann, "Tomographic profiling with Snowscat within the ESA Snowlab campaign: Time series of snow profiles over three snow seasons," in *Proc. IEEE Int. Geosci. Remote Sens. Symp.*, 2018, pp. 6512–6515.

[48] S. Leinss, G. Parrella, and I. Hajnsek, "Snow height determination by polarimetric phase differences in X-band SAR data," *IEEE J. Sel. Topics Appl. Earth Observ. Remote Sens.*, vol. 7, no. 9, pp. 3794–3810, Sep. 2014.

[49] A. G. Fore et al., "UAVSAR polarimetric calibration," *IEEE Trans. Geosci. Remote Sens.*, vol. 53, no. 6, pp. 3481–3491, Jun. 2015.

[50] K. Sarabandi, F. T. Ulaby, and M. A. Tassoudji, "Calibration of polarimetric radar systems with good polarization isolation," *IEEE Trans. Geosci. Remote Sens.*, vol. 28, no. 1, pp. 70–75, Jan. 1990.

[51] P. L. Dekker, H. Rott, P. P. Iraola, B. Chapron, K. Scipal, and E. D. Witte, "Harmony: An Earth explorer 10 mission candidate to observe land, ice, and ocean surface dynamics," in *Proc. IEEE Int. Geosci. Remote Sens. Symp.*, 2019, pp. 8381–8384.

[52] F. Ulaby, K. Sarabandi, and A. Nashashibi, "Statistical properties of the Mueller matrix of distributed targets," *IET Proc. F. Radar Signal Process.*, vol. 139, pp. 136–146 1992. [Online]. Available: https://digital-library.theiet.org/content/journals/10.1049/ip-f-2.1992.0017

[53] M. Migliaccio, F. Nunziata, and A. Gambardella, "On the co-polarized phase difference for oil spill observation," *Int. J. Remote Sens.*, vol. 30, pp. 1587–1602, 2009.

[54] A. Reigber, K. Papathanassiou, M. Jger, and R. Scheiber, "First results of multispectral polarimetry and single-pass POLinSAR with the f-SAR airborne SAR instrument," in *Proc. IEEE Int. Geosci. Remote Sens. Symp.*, 2013, pp. 2305–2308.

[55] E. Everaere, "Polarimetry in bistatic configuration for ultra high frequency radar measurements on forest environment," Ph.D. dissertation, Ecole Polytechnique, Palaiseau, France, 2015.

[56] S. Cloude, *Polarisation: Applications in Remote Sensing*. London, U.K.: Oxford Univ. Press, 2009. [Online]. Available: https://academic.oup.com/book/11554

[57] R. Touzi, "Target scattering decomposition in terms of roll-invariant target parameters," *IEEE Trans. Geosci. Remote Sens.*, vol. 45, no. 1, pp. 73–84, Jan. 2007.

[58] L. Bombrun, "Roll-invariant target decomposition in bistatic polarimetric SAR imagery," *Can. J. Remote Sens.*, vol. 37, pp. 204–212, 2011.

[59] S. E. Park, "Variations of microwave scattering properties by seasonal freeze/thaw transition in the permafrost active layer observed by alos palsar polarimetric data," *Remote Sens.*, vol. 7, pp. 17 135–17 148, 2015.

[60] D. Varade, G. Singh, O. Dikshit, and S. Manickam, "Identification of snow using fully polarimetric SAR data based on entropy and anisotropy," *Water Resour. Res.*, vol. 56, 2020, Art. no. e2019WR025449.

[61] D. Varade, S. Manickam, O. Dikshit, G. Singh, and Snehmani, "Modelling of early winter snow density using fully polarimetric C-band SAR data in the Indian Himalayas," *Remote Sens. Environ.*, vol. 240, 2020, Art. no. 111699.

[62] S. Leinss, A. Wiesmann, J. Lemmetyinen, and I. Hajnsek, "Snow water equivalent of dry snow measured by differential interferometry," *IEEE J. Sel. Topics Appl. Earth Observ. Remote Sens.*, vol. 8, no. 8, pp. 3773–3790, Aug. 2015.

[63] H. A. Zebker and J. Villasenor, "Decorrelation in interferometric radar echoes," *IEEE Trans. Geosci. Remote Sens.*, vol. 30, no. 5, pp. 950–959, Sep. 1992.

[64] R. L. Hawley, E. M. Morris, R. Cullen, U. Nixdorf, A. P. Shepherd, and D. J. Wingham, "ASIRAS airborne radar resolves internal annual layers in the dry-snow zone of Greenland," *Geophys. Res. Lett.*, vol. 33, no. 4, 2006, Art. no. 025147. [Online]. Available: https://agupubs.onlinelibrary.wiley.com/doi/abs/10.1029/2005GL025147

[65] S. Yueh, D. Cline, and K. Elder, "Airborne Ku-band radar remote sensing of terrestrial snow cover," in *Proc. Int. Geosci. Remote Sens. Symp.*, 2007, vol. 47, pp. 1211–1214.

[66] A. Coccia, C. Trampuz, M. Ortolani, R. Turtolo, T. Wieffering, and A. Meta, "Deployment of the SnowSAR sensor in the SnowEx campaign by NASA and preliminary results," in *Proc. IEEE Int. Geosci. Remote Sens. Symp.*, 2017, pp. 1403–1405.
[67] H. M.-J. Cantalloube, "Imaging of snow/ice subsurface features from airborne SAR at UHF, l. and X. band. the Onera SAR campaign in south Greenland," in *Proc. IEEE Int. Geosci. Remote Sens. Symp.*, 2019, pp. 4157–4160.
[68] B. Osmanoglu, R. Rincon, Q. Bonds, P. Racette, L. Brucker, and M. Perrine, "SWESARR: Snow water equivalent radar and radiometer," in *Proc. AGU Fall Meeting Abstr.*, 2018, vol. 2018, pp. C13D–1173.
[69] J. Lemmetyinen et al., "Airborne SnowSAR data at X- and Ku- bands over Boreal forest, alpine and tundra snow cover," *Earth Syst. Sci. Data Discuss.*, vol. 2021, pp. 1–49, 2021. [Online]. Available: https://essd.copernicus.org/preprints/essd-2021-239/
[70] J. M. L. King, R. Kelly, A. Kasurak, C. Duguay, G. Gunn, and J. B. Mead, "UW-Scat: A ground-based dual-frequency scatterometer for observation of snow properties," *IEEE Geosci. Remote Sens. Lett.*, vol. 10, no. 3, pp. 528–532, May 2013.
[71] X. Xu, C. A. Baldi, J.-W. D. Bleser, Y. Lei, S. Yueh, and D. E. Fernandez, "Multi-frequency tomography radar observations of snow stratigraphy at fraser during SnowEx," in *Proc. IEEE Int. Geosci. Remote Sens. Symp.*, 2018, pp. 6269–6272.
[72] X. Xu, H. Shen, H. Xu, and L. Tsang, "Modeling multi-frequency tomograms for snow stratigraphy," in *Proc. IEEE Int. Geosci. Remote Sens. Symp.*, 2020, pp. 3436–3439.
[73] Y. Lei et al., "Dry snow parameter retrieval with ground-based single-pass synthetic aperture radar interferometry," *IEEE Trans. Geosci. Remote Sens.*, vol. 60, Apr. 2022, Art. no. 4304614.
[74] O. Frey, C. L. Werner, R. Caduff, and A. Wiesmann, "A time series of tomographic profiles of a snow pack measured with SnowScat at X-/Ku-band," in *Proc. IEEE Int. Geosci. Remote Sens. Symp.*, 2016, pp. 17–20.
[75] O. Frey, C. L. Werner, R. Caduff, and A. Wiesmann, "Inversion of SNOW structure parameters from time series of tomographic measurements with SnowScat," in *Proc. IEEE Int. Geosci. Remote Sens. Symp.*, 2017, pp. 2472–2475.
[76] C. Werner, O. Frey, R. Naderpour, A. Wiesmann, M. Suess, and U. Wegmüller, "Aperture synthesis and calibration of the WBSCAT ground-based scatterometer," in *Proc. IEEE Int. Geosci. Remote Sens. Symp.*, 2021, pp. 1947–1949.
[77] A. Wiesmann et al., "ESA SnowLab project: 4 years of wide band scatterometer measurements of seasonal snow," in *Proc. IEEE Int. Geosci. Remote Sens. Symp.*, 2019, pp. 5745–5748.
[78] M. Stefko, O. Frey, C. Werner, and I. Hajnsek, "Calibration and operation of a bistatic real-aperture polarimetric-interferometric ku-band radar," *IEEE Trans. Geosci. Remote Sens.*, vol. 60, 2022, Art. no. 5106719.
[79] C. Werner, A. Wiesmann, T. Strozzi, A. Kos, R. Caduff, and U. Wegmüler, "The GPRI multi-mode differential interferometric radar for ground-based observations," in *Proc. 9th Eur. Conf. Synthetic Aperture Radar*, 2012, pp. 304–307.
[80] R. Caduff, A. Kos, F. Schlunegger, B. W. McArdell, and A. Wiesmann, "Terrestrial radar interferometric measurement of hillslope deformation and atmospheric disturbances in the Illgraben debris-flow catchment, Switzerland," *IEEE Geosci. Remote Sens. Lett.*, vol. 11, no. 2, pp. 434–438, Feb. 2014.
[81] T. Strozzi, C. Werner, A. Wiesmann, and U. Wegmuller, "Topography mapping with a portable real-aperture radar interferometer," *IEEE Geosci. Remote Sens. Lett.*, vol. 9, no. 2, pp. 277–281, Mar. 2012.
[82] A. Wiesmann, R. Caduff, and C. Mätzler, "Terrestrial radar observations of dynamic changes in alpine snow," *IEEE J. Sel. Topics Appl. Earth Observ. Remote Sens.*, vol. 8, no. 7, pp. 3665–3671, Jul. 2015.
[83] S. Baffelli, O. Frey, and I. Hajnsek, "Geostatistical analysis and mitigation of the atmospheric phase screens in ku-band terrestrial radar interferometric observations of an alpine glacier," *IEEE Trans. Geosci. Remote Sens.*, vol. 58, no. 11, pp. 7533–7556, Nov. 2020.
[84] Y. Izumi, O. Frey, S. Baffelli, I. Hajnsek, and M. Sato, "Efficient approach for atmospheric phase screen mitigation in time series of terrestrial radar interferometry data applied to measure glacier velocity," *IEEE J. Sel. Topics Appl. Earth Observ. Remote Sens.*, vol. 14, pp. 7734–7750, Jul. 2021.
[85] S. Baffelli, O. Frey, and I. Hajnsek, "Polarimetric analysis of natural terrain observed with a Ku -band terrestrial radar," *IEEE J. Sel. Topics Appl. Earth Observ. Remote Sens.*, vol. 12, no. 12, pp. 5268–5288, Dec. 2019.
[86] G. Jouvet and M. Huss, "Future retreat of great Aletsch glacier," *J. Glaciology*, vol. 65, no. 253, pp. 869–872, 2019.
[87] M. Huss, A. Bauder, M. Funk, and R. Hock, "Determination of the seasonal mass balance of four alpine glaciers since 1865," *J. Geophys. Res.: Earth Surf.*, vol. 113, 2008, Art. no. F000803.
[88] H. Zebker and E. W. Hoen, "Penetration depths inferred from interferometric volume decorrelation observed over the Greenland ice sheet," *IEEE Trans. Geosci. Remote Sens.*, vol. 38, no. 6, pp. 2571–2583, Nov. 2000.
[89] I. McLeod, I. G. Cumming, and M. Seymour, "ENVISAT ASAR data reduction: Impact on SAR interferometry," *IEEE Trans. Geosci. Remote Sens.*, vol. 36, no. 2, pp. 589–602, Mar. 1998.
[90] C. Lucas, S. Leinss, Y. Bühler, A. Marino, and I. Hajnsek, "Multipath interferences in ground-based radar data: A case study," *Remote Sens.*, vol. 9, no. 12, pp. 1–19, 2017.
[91] D. Just and R. Bamler, "Phase statistics of interferograms with applications to synthetic aperture radar," *Appl. Opt.*, vol. 33, no. 20, pp. 4361–4368, Jul. 1994. [Online]. Available: https://www.osapublishing.org/abstract.cfm?URI=ao-33-20-4361
[92] H. H. Ku, "Notes on the use of propagation of error formulas," *J. Res. Nat. Bur. Standards*, vol. 70, no. 4, pp. 263–273, 1966.
[93] S. Baffelli, O. Frey, C. Werner, and I. Hajnsek, "Polarimetric calibration of the Ku-band advanced polarimetric radar interferometer," *IEEE Trans. Geosci. Remote Sens.*, vol. 56, no. 4, pp. 2295–2311, Apr. 2017.
[94] I. Hajnsek, K. P. Papathanassiou, and S. R. Cloude, "Removal of additive noise in polarimetric eigenvalue processing," in *Proc. Scanning Present Resolving Future. Proc. IEEE Int. Geosci. Remote Sens. Symp.*, 2001, vol. 6, pp. 2778–2780.
[95] E. J. Rignot, "Backscatter model for the unusual radar properties of the Greenland ice sheet," *J. Geophys. Res.*, vol. 100, no. E5, pp. 9389–9400, 1995.
[96] P. Chang, J. Mead, E. Knapp, G. Sadowy, R. Davis, and R. McIntosh, "Polarimetric backscatter from fresh and metamorphic snowcover at millimeter wavelengths," *IEEE Trans. Antennas Propag.*, vol. 44, no. 1, pp. 58–73, Jan. 1996.
[97] K. Belinska, G. Fischer, T. Nagler, and I. Hajnsek, "Snow water equivalent estimation using differential SAR interferometry and co-polar phase differences from airborne SAR data," in *Proc. Int. Geosci. Remote Sens. Symp.*, 2022, pp. 4545–4548.
[98] R. Millan, J. Mouginot, A. Rabatel, and M. Morlighem, "Ice velocity and thickness of the world's glaciers," *Nature Geosci.*, vol. 15, pp. 124–129, 2022.
[99] J. J. Ruiz et al., "Investigation of environmental effects on coherence loss in SAR interferometry for snow water equivalent retrieval," *IEEE Trans. Geosci. Remote Sens.*, vol. 60, Nov. 2022, Art. no. 4306715.
[100] G. Parrella, I. Hajnsek, and K. P. Papathanassiou, "Polarimetric decomposition of L-band PolSAR backscattering over the Austfonna ice cap," *IEEE Trans. Geosci. Remote Sens.*, vol. 54, no. 3, pp. 1267–1281, Mar. 2016.

Marcel Stefko (Member, IEEE) received the M.Sc. degree in applied physics from the École Polytechnique Fédérale de Lausanne (EPFL), Lausanne, Switzerland, in 2017, and the Ph.D. (Dr.Sc.) degree in radar remote sensing from ETH Zurich, Zurich, Switzerland, in 2023.

From 2017 to 2018, he was a Young Graduate Trainee with the European Space Agency, Noordwijk, The Netherlands. He is currently with the Chair of Earth Observation and Remote Sensing, ETH Zrich. His Ph.D. work focused on the development of calibration, data acquisition, and data processing methods for bistatic radar systems, as well as exploration of potential applications of these systems in natural environments. His current research focuses on exploitation of bistatic radar systems for monitoring of snow-covered environments.

Philipp Bernhard received the M.Sc. degree in physics in 2016 from ETH Zürich, Zrich, Switzerland, where he is currently working toward the Ph.D. degree, focusing on the quantification of permafrost thaw in the Arctic using TanDEM-X observations.

He is currently a Postdoctoral Researcher with ETH Zürich, working on Persistent Scatterer Analysis for railway infrastructure monitoring. He is with Gamma Remote Sensing, focusing on SAR-driven applications. His Ph.D. work involved creating digital elevation models, processing SAR data, and merging different remote sensing products for widespread application. His research focuses on remote sensing significantly aids both environmental study and infrastructure monitoring efforts.

Othmar Frey (Senior Member, IEEE) received the M.Sc. degree in geomatic engineering from ETH Zürich, Zürich, Switzerland, in 2002, and the Ph.D. (Dr.sc.nat.) degree in radar remote sensing from the University of Zurich, Zürich, in 2010.

From 2002 to 2010, he was a Research Associate with the Remote Sensing Laboratory, University of Zurich. He has been a PI or a Co-Investigator in various national and international research projects. Recently, he was the PI of an Innosuisse Project in which a new car- and unmanned aerial vehicle (UAV)-borne interferometric synthetic aperture radar (InSAR) system for mobile mapping of surface displacements has been developed. At Gamma Remote Sensing, Gümligen, Switzerland, he has also been active in the development of the Gamma Software and in technical/scientific consulting on synthetic aperture radar (SAR) imaging and interferometric applications to European Space Agency (ESA), National Aeronautics and Space Administration (NASA), and aerospace industry. He is currently a Tenured Senior Scientist and a Lecturer with ETH Zrich and also a Senior Scientist with Gamma Remote Sensing. His research interests include 2-D and 3-D (tomographic) SAR imaging and interferometric/polarimetric techniques and application development, including 3-D forest mapping, ground motion, geohazard monitoring, and snow parameter retrieval profiling using spaceborne, airborne, UAV-borne, and terrestrial radar sensors.

Dr. Frey was a Member of the Satlite Argentino de Observación Con Microondas-Companion Satellite (SAOCOM-CS) Science Expert Group with the European Space Agency. He was the recipient of the ETH Medal for the M.Sc. thesis and the Distinction Award from the Faculty of Science for the Ph.D. degree. Since 2015, he has been the Chair of the Swiss Chapter of the IEEE Geoscience and Remote Sensing Society.

Irena Hajnsek (Fellow Member, IEEE) received the Dipl. (Hons.) degree in fluvial river systems from the Free University of Berlin, Berlin, Germany, in 1996, and the Dr. rer. nat. (Hons.) degree in model-based estimation of soil moisture from fully polarimetric synthetic aperture radar from Friedrich Schiller University Jena, Jena, Germany, in 2001.

Since 2009, she has been a Professor of Earth observation with the Institute of Environmental Engineering, Swiss Federal Institute of Technology (ETH), Zürich, Switzerland, and the Head of the Polarimetric SAR Interferometry research group at the Microwaves and Radar Institute, German Aerospace Center, Koeln, Germany. Since 2010, she has been the Science Coordinator of the German satellite mission TanDEM-X. Her research interests include electromagnetic propagation and scattering theory, radar polarimetry, SAR and interferometric SAR data processing techniques, and environmental parameter modeling and estimation.

Dr. Hajnsek is a Member of the European Space Agency Mission Advisory Group for the ROSE-L Mission. She was the Technical Program Co-Chair of the IEEE IGARSS 2012 in Munich, Germany, and in Yokohama, Japan, in 2019. From 2013 to 2021, she was a Member of the IEEE GRSS AdCom, and from 2016 to 2020, she was the Vice President of the IEEE GRSS Technical Committees. She is the Founder of the new Technical Committee Remote sensing Environment, Analysis and Climate Technologies (REACT) that exists since November 2021.